PHYSICAL REVIEW D **109,** 072014 (2024)

Atmospheric neutrino oscillation analysis with neutron tagging and an expanded fiducial volume in Super-Kamiokande I–V

T. Wester,[4,*] K. Abe,[1,44] C. Bronner,[1] Y. Hayato,[1,44] K. Hiraide,[1,44] K. Hosokawa,[1] K. Ieki,[1,44] M. Ikeda,[1,44]
J. Kameda,[1,44] Y. Kanemura,[1] R. Kaneshima,[1] Y. Kashiwagi,[1] Y. Kataoka,[1,44] S. Miki,[1] S. Mine,[1,6] M. Miura,[1,44]
S. Moriyama,[1,44] Y. Nakano,[1] M. Nakahata,[1,44] S. Nakayama,[1,44] Y. Noguchi,[1] K. Sato,[1] H. Sekiya,[1,44] H. Shiba,[1]
K. Shimizu,[1] M. Shiozawa,[1,44] Y. Sonoda,[1] Y. Suzuki,[1] A. Takeda,[1,44] Y. Takemoto,[1,44] H. Tanaka,[1,44] T. Yano,[1]
S. Han,[2] T. Kajita,[2,44,22] K. Okumura,[2,44] T. Tashiro,[2] T. Tomiya,[2] X. Wang,[2] S. Yoshida,[2] P. Fernandez,[3] L. Labarga,[3]
N. Ospina,[3] B. Zaldivar,[3] B. W. Pointon,[5,47] E. Kearns,[4,44] J. L. Raaf,[4] L. Wan,[4] J. Bian,[6] N. J. Griskevich,[6]
S. Locke,[6] M. B. Smy,[6,44] H. W. Sobel,[6,44] V. Takhistov,[6,24] A. Yankelevich,[6] J. Hill,[7] S. H. Lee,[8] D. H. Moon,[8]
R. G. Park,[8] B. Bodur,[9] K. Scholberg,[9,44] C. W. Walter,[9,44] A. Beauchêne,[10] O. Drapier,[10] A. Giampaolo,[10]
Th. A. Mueller,[10] A. D. Santos,[10] P. Paganini,[10] B. Quilain,[10] T. Nakamura,[11] J. S. Jang,[12] L. N. Machado,[13]
J. G. Learned,[14] K. Choi,[15] N. Iovine,[15] S. Cao,[16] L. H. V. Anthony,[17] D. Martin,[17] N. W. Prouse,[17] M. Scott,[17]
A. A. Sztuc,[17] Y. Uchida,[17] V. Berardi,[18] M. G. Catanesi,[18] E. Radicioni,[18] N. F. Calabria,[19] A. Langella,[19]
G. De Rosa,[19] G. Collazuol,[20] F. Iacob,[20] M. Mattiazzi,[20] L. Ludovici,[21] M. Gonin,[22] G. Pronost,[22] C. Fujisawa,[23]
Y. Maekawa,[23] Y. Nishimura,[23] R. Okazaki,[23] R. Akutsu,[24] M. Friend,[24] T. Hasegawa,[24] T. Ishida,[24] T. Kobayashi,[24]
M. Jakkapu,[24] T. Matsubara,[24] T. Nakadaira,[24] K. Nakamura,[24,44] Y. Oyama,[24] K. Sakashita,[24] T. Sekiguchi,[24]
T. Tsukamoto,[24] N. Bhuiyan,[25] G. T. Burton,[25] F. Di Lodovico,[25] J. Gao,[25] A. Goldsack,[25] T. Katori,[25] J. Migenda,[25]
R. Ramsden,[25] Z. Xie,[25] S. Zsoldos,[25,44] A. T. Suzuki,[26] Y. Takagi,[26] Y. Takeuchi,[26,44] H. Zhong,[26] J. Feng,[27] L. Feng,[27]
J. R. Hu,[27] Z. Hu,[27] M. Kawaue,[27] T. Kikawa,[27] M. Mori,[27] T. Nakaya,[27,44] R. A. Wendell,[27,44] K. Yasutome,[27]
S. J. Jenkins,[28] N. McCauley,[28] P. Mehta,[28] A. Tarrant,[28] Y. Fukuda,[29] Y. Itow,[30,31] H. Menjo,[30] K. Ninomiya,[30]
J. Lagoda,[32] S. M. Lakshmi,[32] M. Mandal,[32] P. Mijakowski,[32] Y. S. Prabhu,[32] J. Zalipska,[32] M. Jia,[33] J. Jiang,[33] C. K. Jung,[33]
W. Shi,[33] M. J. Wilking,[33] C. Yanagisawa,[33,†] M. Harada,[34] Y. Hino,[34] H. Ishino,[34] Y. Koshio,[34,44] F. Nakanishi,[34]
S. Sakai,[34] T. Tada,[34] T. Tano,[34] T. Ishizuka,[35] G. Barr,[36] D. Barrow,[36] L. Cook,[36,44] A. Holin,[36] F. Nova,[36] S. Samani,[36]
D. Wark,[36] S. Jung,[37] B. S. Yang,[37] J. Y. Yang,[37] J. Yoo,[37] J. E. P. Fannon,[38] L. Kneale,[38] M. Malek,[38]
J. M. McElwee,[38] M. D. Thiesse,[38] L. F. Thompson,[38] S. T. Wilson,[38] H. Okazawa,[39] S. B. Kim,[40] E. Kwon,[40]
J. W. Seo,[40] I. Yu,[40] A. K. Ichikawa,[41] K. D. Nakamura,[41] S. Tairafune,[41] K. Nishijima,[42] A. Eguchi,[43]
K. Nakagiri,[43] Y. Nakajima,[43,44] S. Shima,[43] N. Taniuchi,[43] E. Watanabe,[43] M. Yokoyama,[43,44] P. de Perio,[44]
S. Fujita,[44] K. Martens,[44] K. M. Tsui,[44] M. R. Vagins,[44,6] J. Xia,[44] S. Izumiyama,[45] M. Kuze,[45] R. Matsumoto,[45]
M. Ishitsuka,[46] H. Ito,[46] Y. Ommura,[46] N. Shigeta,[46] M. Shinoki,[46] K. Yamauchi,[46] T. Yoshida,[46] R. Gaur,[47]
V. Gousy-Leblanc,[47,‡] M. Hartz,[47] A. Konaka,[47] X. Li,[47] S. Chen,[48] B. D. Xu,[48] B. Zhang,[48] M. Posiadala-Zezula,[49]
S. B. Boyd,[50] R. Edwards,[50] D. Hadley,[50] M. Nicholson,[50] M. O'Flaherty,[50] B. Richards,[50] A. Ali,[51,47] B. Jamieson,[51]
S. Amanai,[52] Ll. Marti,[52] A. Minamino,[52] and S. Suzuki[52]

(The Super-Kamiokande Collaboration)

[1]*Kamioka Observatory, Institute for Cosmic Ray Research, University of Tokyo,
Kamioka, Gifu 506-1205, Japan*
[2]*Research Center for Cosmic Neutrinos, Institute for Cosmic Ray Research, University of Tokyo,
Kashiwa, Chiba 277-8582, Japan*
[3]*Department of Theoretical Physics, University Autonoma Madrid, 28049 Madrid, Spain*
[4]*Department of Physics, Boston University, Boston, Massachusetts 02215, USA*
[5]*Department of Physics, British Columbia Institute of Technology,
Burnaby, British Columbia V5G 3H2, Canada*
[6]*Department of Physics and Astronomy, University of California,
Irvine, Irvine, California 92697-4575, USA*
[7]*Department of Physics, California State University, Dominguez Hills, Carson, California 90747, USA*
[8]*Institute for Universe and Elementary Particles, Chonnam National University, Gwangju 61186, Korea*
[9]*Department of Physics, Duke University, Durham, North Carolina 27708, USA*
[10]*Ecole Polytechnique, IN2P3-CNRS, Laboratoire Leprince-Ringuet, F-91120 Palaiseau, France*
[11]*Department of Physics, Gifu University, Gifu, Gifu 501-1193, Japan*
[12]*GIST College, Gwangju Institute of Science and Technology, Gwangju 500-712, Korea*
[13]*School of Physics and Astronomy, University of Glasgow, Glasgow G12 8QQ, United Kingdom*
[14]*Department of Physics and Astronomy, University of Hawaii, Honolulu, Hawaii 96822, USA*
[15]*Center for Underground Physics, Institute for Basic Science (IBS), Daejeon 34126, Korea*

2470-0010/2024/109(7)/072014(24)

Published by the American Physical Society

[16]*Institute For Interdisciplinary Research in Science and Education, ICISE, Quy Nhon 55121, Vietnam*
[17]*Department of Physics, Imperial College London, London SW7 2AZ, United Kingdom*
[18]*Dipartimento Interuniversitario di Fisica, INFN Sezione di Bari*
and Università e Politecnico di Bari, I-70125, Bari, Italy
[19]*Dipartimento di Fisica, INFN Sezione di Napoli and Università di Napoli, I-80126, Napoli, Italy*
[20]*Dipartimento di Fisica, INFN Sezione di Padova and Università di Padova, I-35131, Padova, Italy*
[21]*INFN Sezione di Roma and Università di Roma "La Sapienza," I-00185, Roma, Italy*
[22]*ILANCE, CNRS—University of Tokyo International Research Laboratory,*
Kashiwa, Chiba 277-8582, Japan
[23]*Department of Physics, Keio University, Yokohama, Kanagawa 223-8522, Japan*
[24]*High Energy Accelerator Research Organization (KEK), Tsukuba, Ibaraki 305-0801, Japan*
[25]*Department of Physics, King's College London, London WC2R 2LS, United Kingdom*
[26]*Department of Physics, Kobe University, Kobe, Hyogo 657-8501, Japan*
[27]*Department of Physics, Kyoto University, Kyoto, Kyoto 606-8502, Japan*
[28]*Department of Physics, University of Liverpool, Liverpool L69 7ZE, United Kingdom*
[29]*Department of Physics, Miyagi University of Education, Sendai, Miyagi 980-0845, Japan*
[30]*Institute for Space-Earth Environmental Research, Nagoya University, Nagoya, Aichi 464-8602, Japan*
[31]*Kobayashi-Maskawa Institute for the Origin of Particles and the Universe, Nagoya University,*
Nagoya, Aichi 464-8602, Japan
[32]*National Centre for Nuclear Research, 02-093 Warsaw, Poland*
[33]*Department of Physics and Astronomy, State University of New York at Stony Brook,*
New York 11794-3800, USA
[34]*Department of Physics, Okayama University, Okayama, Okayama 700-8530, Japan*
[35]*Media Communication Center, Osaka Electro-Communication University,*
Neyagawa, Osaka 572-8530, Japan
[36]*STFC Rutherford Appleton Laboratory, Harwell, Oxford OX11 0QX, United Kingdom*
[37]*Department of Physics, Seoul National University, Seoul 151-742, Korea*
[38]*Department of Physics and Astronomy, University of Sheffield, Sheffield S3 7RH, United Kingdom*
[39]*Department of Informatics in Social Welfare, Shizuoka University of Welfare,*
Yaizu, Shizuoka 425-8611, Japan
[40]*Department of Physics, Sungkyunkwan University, Suwon 440-746, Korea*
[41]*Department of Physics, Faculty of Science, Tohoku University, Sendai, Miyagi 980-8578, Japan*
[42]*Department of Physics, Tokai University, Hiratsuka, Kanagawa 259-1292, Japan*
[43]*Department of Physics, University of Tokyo, Bunkyo, Tokyo 113-0033, Japan*
[44]*Kavli Institute for the Physics and Mathematics of the Universe (WPI), The University of Tokyo Institutes*
for Advanced Study, University of Tokyo, Kashiwa, Chiba 277-8583, Japan
[45]*Department of Physics, Tokyo Institute of Technology, Meguro, Tokyo 152-8551, Japan*
[46]*Department of Physics, Faculty of Science and Technology, Tokyo University of Science,*
Noda, Chiba 278-8510, Japan
[47]*TRIUMF, 4004 Wesbrook Mall, Vancouver, British Columbia V6T2A3, Canada*
[48]*Department of Engineering Physics, Tsinghua University, Beijing 100084, China*
[49]*Faculty of Physics, University of Warsaw, Warsaw 02-093, Poland*
[50]*Department of Physics, University of Warwick, Coventry CV4 7AL, United Kingdom*
[51]*Department of Physics, University of Winnipeg, Manitoba R3J 3L8, Canada*
[52]*Department of Physics, Yokohama National University,*
Yokohama, Kanagawa 240-8501, Japan

(Received 9 November 2023; accepted 14 February 2024; published 24 April 2024)

We present a measurement of neutrino oscillation parameters with the Super-Kamiokande detector using atmospheric neutrinos from the complete pure-water SK I–V (April 1996–July 2020) dataset, including events from an expanded fiducial volume. The dataset corresponds to 6511.3 live days and an exposure of

---

[*]Corresponding author: twester@bu.edu
[†]Also at BMCC/CUNY, Science Department, New York, New York, 1007, USA.
[‡]Also at University of Victoria, Department of Physics and Astronomy, P.O. Box 1700 STN CSC, Victoria, British Columbia V8W 2Y2, Canada.

484.2 kiloton-years. Measurements of the neutrino oscillation parameters Δm^2_{32}, $\sin^2\theta_{23}$, $\sin^2\theta_{13}$, δ_{CP}, and the preference for the neutrino mass ordering are presented with atmospheric neutrino data alone, and with constraints on $\sin^2\theta_{13}$ from reactor neutrino experiments. Our analysis including constraints on $\sin^2\theta_{13}$ favors the normal mass ordering at the 92.3% level.

DOI: 10.1103/PhysRevD.109.072014

I. INTRODUCTION

Neutrino oscillations in the Pontecorvo-Maki-Nakagawa-Sakata (PMNS) paradigm are parametrized by three mixing angles, two squared-mass differences, and a CP-violating phase [1,2]. Experiments measuring neutrinos of different flavors, energies, and baselines have constrained many of the PMNS parameters with increasing levels of precision. However, the octant of the mixing angle θ_{23}, the phase δ_{CP}, and the sign of the larger of the two squared-mass differences, Δm^2_{32}, which determines the neutrino mass ordering, are all presently unknown. To date, the long-baseline accelerator neutrino experiments T2K [3] and NOvA [4] have made the world's most precise measurements of θ_{23}, Δm^2_{32}, and δ_{CP}, but they have yet to definitively resolve the remaining questions.

Atmospheric neutrinos are an independent and natural counterpart to accelerator neutrinos for studying neutrino oscillations. Neutrinos created in the Earth's atmosphere span a range of energies and baselines that make their oscillations sensitive to the θ_{23} mixing angle and the magnitude of the Δm^2_{32} squared-mass difference. Additionally, atmospheric neutrinos which pass near or through the dense core of the Earth experience matter effects which alter their oscillation probabilities. An observation of these modified oscillation probabilities in either atmospheric neutrino or antineutrino data would provide important information toward resolving the neutrino mass ordering.

In this work, we analyze 6511.3 live days of atmospheric neutrino data from the Super-Kamiokande (SK) detector. This analysis improves upon the previous work [5] in three major ways: We use the number of tagged neutrons to enhance the separation of neutrino events from antineutrino events, we enhance the efficiency of classifying multi-ring events using a boosted decision tree (BDT), and we add 48% exposure by analyzing events from an expanded fiducial volume and from 1186 additional live days, including data collected after a major detector refurbishment in 2018. In addition to the atmospheric-only analysis, we present an analyses of SK data with an external constraint on the mixing angle θ_{13} from the average measurements of the reactor neutrino experiments Daya Bay [6], RENO [7], and Double-Chooz [8].

The paper is organized as follows: Section I presents an overview of neutrino oscillation phenomenology relevant to atmospheric neutrino oscillations. Section II provides a description of the Super-Kamiokande detector and its capabilities for reconstructing neutrino interactions. Section III describes the simulation used to model atmospheric neutrinos interactions at SK. Section IV describes the analysis methodology and presents the results of the analyses without external constraints and with constraints on $\sin^2\theta_{13}$. We provide an interpretation and summary of the results in Sec. V.

A. Neutrino oscillations

Neutrinos are produced as flavor eigenstates of the weak interaction, which may be treated as superpositions of mass eigenstates via the PMNS matrix:

$$|\nu_\alpha\rangle = \sum_{i=1}^{3} \mathbf{U}^*_{\alpha i}|\nu_i\rangle, \tag{1}$$

where α is a label for each lepton flavor—one of e, μ, or τ—and $\mathbf{U}_{\alpha i}$ is an element of the PMNS matrix. The PMNS matrix is parametrized by three mixing angles and a phase, and it factorizes into three submatrices which describe rotations by each mixing angle from the neutrino mass basis into the neutrino flavor basis:

$$\mathbf{U} = \begin{pmatrix} 1 & 0 & 0 \\ 0 & c_{23} & s_{23} \\ 0 & -s_{23} & c_{23} \end{pmatrix} \begin{pmatrix} c_{13} & 0 & s_{13}e^{-i\delta_{\mathrm{CP}}} \\ 0 & 1 & 0 \\ -s_{13}e^{i\delta_{\mathrm{CP}}} & 0 & c_{13} \end{pmatrix} \times \begin{pmatrix} c_{12} & s_{12} & 0 \\ -s_{12} & c_{12} & 0 \\ 0 & 0 & 1 \end{pmatrix}. \tag{2}$$

In Eq. (2), the sines and cosines of the mixing angles are written as $\cos\theta_{ij} \equiv c_{ij}$ and $\sin\theta_{ij} \equiv s_{ij}$, respectively, and the phase δ_{CP} changes sign for the antineutrino case. The probability of a neutrino of one flavor $|\nu_\alpha\rangle$ oscillating to a different flavor $|\nu_\beta\rangle$ after some time t—or, equivalently, along a baseline L—is found by computing the amplitude $|\langle\nu_\beta|\nu_\alpha\rangle|^2$. The probability is nonzero for the case $\alpha \neq \beta$ if the mass states have nonzero mass differences given by the signed quantity $\Delta m^2_{ij} = m^2_i - m^2_j$.

In the simplest case, neutrinos oscillate in a vacuum, and oscillation probabilities may be computed by propagating neutrino states according to their vacuum Hamiltonian, written here in the mass basis:

$$H_{\text{Vacuum}} = \begin{pmatrix} \frac{m_1^2}{2E} & 0 & 0 \\ 0 & \frac{m_2^2}{2E} & 0 \\ 0 & 0 & \frac{m_3^2}{2E} \end{pmatrix}. \quad (3)$$

This leads to oscillation probabilities of the form

$$P_{\alpha\to\beta} = \delta_{\alpha\beta} - 4\sum_{i>j}\text{Re}(U_{\alpha i}^{*}U_{\beta i}U_{\alpha j}U_{\beta j}^{*})\sin^2\Delta_{ij} \pm 2\sum_{i>j}\text{Im}(U_{\alpha i}^{*}U_{\beta i}U_{\alpha j}U_{\beta j}^{*})\sin 2\Delta_{ij}, \quad (4)$$

where $\Delta_{ij} = 1.27\Delta m_{ij}^2 L/E$. Here, Δm_{ij}^2 is expressed in units of eV^2, L is the oscillation baseline in kilometers, and E is the neutrino energy in GeV. Experiments have measured all mixing angles and squared-mass differences to be significantly different from zero, while the value of the phase δ_{CP} is still unknown.[1] In addition, solar neutrino oscillation experiments observe evidence for matter effects in the Sun which imply that the Δm_{21}^2 squared-mass difference is positive, establishing an ordering for two of the neutrino masses, $m_2 > m_1$ [9–12]. However, current experiments are consistent with either the *normal* ordering, $m_3 \gg m_2, m_1$, or the *inverted* ordering, $m_2, m_1 \gg m_3$. Consequently, the sign of the squared-mass difference between m_3 and the next-most-massive neutrino, given by either Δm_{32}^2 or Δm_{31}^2, is not known. We use the notation $\Delta m_{32,31}^2$ or simply Δm^2 for this squared-mass difference where the ordering is not explicitly specified.

Numerically, $\Delta m_{32,31}^2$ has been measured to be approximately 30 times larger than Δm_{21}^2, such that $\Delta m_{32}^2 \approx \Delta m_{31}^2$. The difference in magnitude between Δm_{21}^2 and $\Delta m_{32,31}^2$ also implies that the terms in Eq. (4) containing one or the other squared-mass differences dominate for different ranges of L/E. For long-baseline beam and atmospheric neutrinos, where neutrino baselines range from tens of kilometers to several thousand kilometers, and typical neutrino energies range from MeV to several GeV, the Δm_{21}^2 terms are subdominant, leading to approximate flavor oscillation probabilities of the form

$$\begin{aligned} P(\nu_\mu \leftrightarrow \nu_e) &\approx \sin^2\theta_{23}\sin^2 2\theta_{13}\sin^2\left(1.27\frac{\Delta m^2 L}{E}\right), \\ P(\nu_\mu \to \nu_\mu) &\approx 1 - 4\cos^2\theta_{13}\sin^2\theta_{23}(1-\cos^2\theta_{13}\sin^2\theta_{23}) \\ &\quad \times \sin^2\left(1.27\frac{\Delta m^2 L}{E}\right), \\ P(\nu_e \to \nu_e) &\approx 1 - \sin^2 2\theta_{13}\sin^2\left(1.27\frac{\Delta m^2 L}{E}\right). \end{aligned} \quad (5)$$

The approximate oscillation probabilities in Eq. (5) are primarily functions of the mixing angles and the absolute value of the squared-mass difference Δm^2. The phase δ_{CP}, and the neutrino mass ordering—i.e., the sign of the squared-mass difference—are subleading effects which make them challenging experimental signatures.

Neutrino oscillations in matter enhance the dependence of oscillation probabilities on the neutrino mass ordering. In matter, due to an increased forward scattering amplitude, electron-flavor neutrinos experience a larger potential relative to μ and τ flavors, which modifies the vacuum Hamiltonian via an additional term,

$$H_{\text{Matter}} = H_{\text{Vacuum}} + \mathbf{U}^{\dagger}\begin{pmatrix} a & 0 & 0 \\ 0 & 0 & 0 \\ 0 & 0 & 0 \end{pmatrix}\mathbf{U}, \quad (6)$$

where $a = \pm\sqrt{2}G_F N_e$. Here, G_F is the Fermi constant, N_e is the electron density, and $\mathbf{U}$ is the PMNS matrix. The sign of a is positive for neutrinos and negative for antineutrinos. Propagating the neutrino states according to the matter Hamiltonian leads to an effective squared-mass difference and mixing angle:

$$\begin{aligned} \Delta m_{\text{M}}^2 &= \Delta m^2\sqrt{\sin^2 2\theta_{13} + (\Gamma - \cos 2\theta_{13})^2}, \\ \sin^2 2\theta_{13,\text{M}} &= \frac{\sin^2 2\theta_{13}}{\sin^2 2\theta_{13} + (\Gamma - \cos 2\theta_{13})^2}, \end{aligned} \quad (7)$$

where $\Gamma \equiv 2aE/\Delta m^2$. Equation (7) shows that the effective quantities depend on the sign of Δm^2. In particular, for neutrinos in the normal ordering, $\Gamma \approx \cos 2\theta_{13}$ maximizes the effective mixing angle $\sin^2\theta_{13,\text{M}}$. A maximum also occurs for antineutrinos in the inverted ordering. This maximum effective mixing angle predicts a resonant enhancement of muon-to-electron flavor conversions for either neutrinos or antineutrinos according to the neutrino mass ordering.

B. Atmospheric neutrinos

Atmospheric neutrinos are produced when cosmic rays interact with nuclei in the Earth's atmosphere. These interactions result in hadronic showers of primarily pions and kaons, which decay into neutrinos. The atmospheric neutrino energy spectrum extends from a few MeV to several TeV and has an approximate flavor ratio in the few-GeV range of $(\nu_\mu + \bar{\nu}_\mu)/(\nu_e + \bar{\nu}_e) \approx 2{:}1$. While present, tau neutrinos intrinsic to the atmospheric neutrino flux are suppressed by many orders of magnitude relative to electron- and muon-flavor neutrinos due to kinematic restrictions on their production.

The zenith angle θ_z describes atmospheric neutrino baselines. Neutrinos produced directly above a detector are downward-going, $\theta_z = 0$, and are produced at an

---

[1] Recent results from T2K favor maximal *CP* violation, $\delta_{\text{CP}} \approx -\pi/2$ [3], while recent measurements from NOvA disfavor *CP*-violating scenarios [4].

TABLE I. Neutrino propagation layers and corresponding densities used for calculating neutrino oscillation probabilities in this analysis, based on a simplified PREM [13].

Layer	R_{Min} (km)	R_{Max} (km)	Density $(\mathrm{g/cm^3})$
Atmosphere	6371	⋯	0
Crust	5701	6371	3.3
Mantle	3480	5701	5.0
Outer core	1220	3480	11.3
Inner core	0	1220	13.0

average distance of 15 km above Earth's surface. Neutrinos produced on the other side of the Earth from a detector are upward-going, $\theta_z = \pi$, and travel an approximate distance of 13 000 km through the Earth. Oscillation signatures are most evident in upward-going atmospheric neutrinos due to the longer baselines.

A general atmospheric neutrino baseline begins at a production point in the atmosphere and passes through the Earth before ending at a detector near the surface. We model the matter effects induced by passage through the Earth assuming a simplified version of the preliminary reference Earth model (PREM) [13], where the Earth is treated as a sphere with radius $R_{\mathrm{Earth}} = 6371$ km and contains concentric spherical shells of decreasing densities. Table I lists the Earth layers and corresponding densities assumed in this work.

To compute neutrino oscillation amplitudes through layers of different matter densities, amplitudes along steps through matter of fixed densities are multiplied together [14]. The general matrix form of the propagated mass eigenvectors $\mathbf{X}$ for neutrinos passing through a fixed matter density is

$$\mathbf{X} = \sum_k \left[\prod_{j\neq k} \frac{2EH_{\mathrm{Matter}} - M_j^2 \mathbf{I}}{M_k^2 - M_j^2}\right] \exp\left(-i\frac{M_k^2 L}{2E}\right), \quad (8)$$

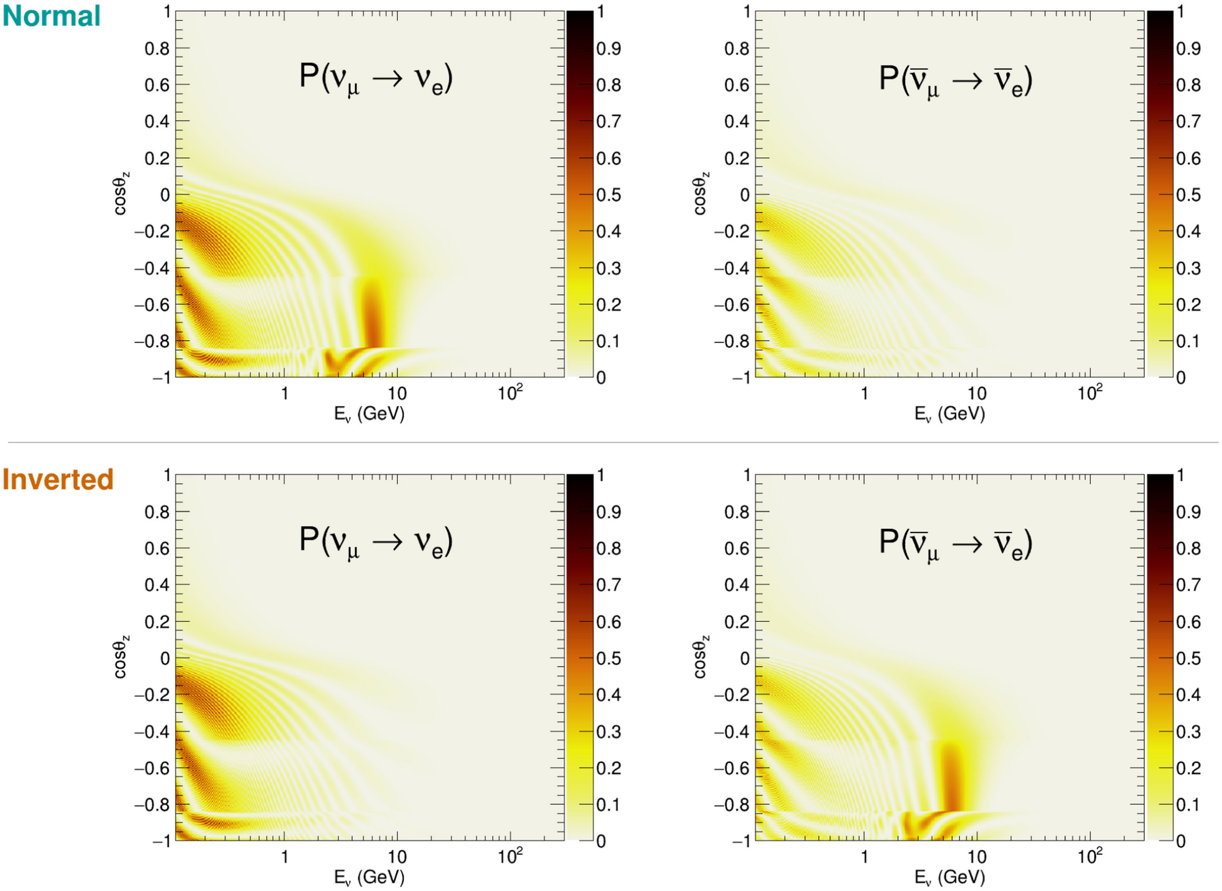

FIG. 1. Electron-to-muon flavor oscillation probabilities of atmospheric neutrinos as a function of cosine zenith angle and neutrino energy. The top row shows the probabilities for neutrinos and antineutrinos in the normal mass-ordering scenario, and the bottom row shows the same probabilities for the inverted mass-ordering scenario. The probabilities are calculated assuming $\sin^2\theta_{23} = 0.5$, $\sin^2\theta_{13} = 0.022$, $\sin^2\theta_{12} = 0.307$, $|\Delta m^2_{32,31}| = 2.4\times10^{-3}\ \mathrm{eV}^2$, $\Delta m^2_{21} = 7.53\times10^{-5}\ \mathrm{eV}^2$, and $\delta_{\mathrm{CP}} = -\pi/2$. The matter effect resonance is visible in the normal ordering for neutrinos (upper left) or the inverted ordering for antineutrinos (lower right) between 2 GeV and 10 GeV, and for $\cos\theta_z \lesssim -0.5$.

where $M_i^2/2E$ are the eigenvalues of H_{Matter}. This definition allows the neutrino probability along a baseline of changing matter density to be written as

$$P(\nu_\alpha \to \nu_\beta) = \left| \left(\mathbf{U} \prod_i \mathbf{X}(E, \rho_i, L_i) \mathbf{U}^\dagger \right)_{\alpha\beta} \right|^2, \qquad (9)$$

where L_i and ρ_i are the baseline and density of the ith step, respectively. In the case of a spherically symmetric Earth, as is assumed in this work, the neutrino oscillation baseline L only depends on the zenith angle and production height and does not depend on the azimuth.

Figure 1 shows the calculated oscillation probabilities for atmospheric neutrinos as a function of the cosine of the zenith angle and the neutrino energy E_ν. The two sets of figures show the cases for muon- to electron-flavor neutrino and antineutrino oscillation probabilities in each mass-ordering scenario. The resonance in $\nu_\mu \to \nu_e$ or $\bar{\nu}_\mu \to \bar{\nu}_e$ oscillations due to matter effects is exclusively visible in the normal and inverted scenarios, respectively, and occurs at baselines of several thousand kilometers and neutrino energies around a few GeV. This resonance in atmospheric neutrinos is the experimental signature of the unknown neutrino mass ordering.

In addition to mass-ordering sensitivity via Earth matter effects, atmospheric neutrino oscillations also provide sensitivity to other oscillation parameters. Muon-to-tau flavor conversions provide sensitivity to $|\Delta m^2_{32,31}|$ and $\sin^2\theta_{23}$. While the tau neutrinos are often too low-energy to produce CC interactions, the $P(\nu_\mu \to \nu_\mu)$ survival probability manifests as a disappearance of upward-going muon neutrinos. Atmospheric neutrinos also provide modest sensitivity to the combined effects of δ_{CP} and $\sin^2\theta_{13}$ through electron neutrino or antineutrino appearance for neutrinos of all energies.

II. THE SUPER-KAMIOKANDE DETECTOR

Super-Kamiokande (SK) is a 50 kiloton cylindrical water-Cherenkov detector located within the Kamioka mine in Gifu, Japan [15,16]. The detector consists of two optically separated regions: an inner detector (ID), which contains 32 kilotons of water and is viewed by over 11 000 inward-facing 20-inch photomultiplier tubes (PMTs), and a 2 m–thick outer detector (OD) with over 1800 outward-facing 8-inch PMTs for vetoing cosmic backgrounds. To increase the light collected in the OD, the OD walls are covered with reflective Tyvek, and wavelength-shifting plates are mounted to the OD PMTs. The ID PMTs have typical quantum efficiencies of 20% for wavelengths near 400 nm and timing resolutions of 2 ns for 1 photoelectron [17].

SK has been operational since its construction in 1996 and, until July 2020, has operated with pure water. During this period, there were five distinct data-taking phases, SK I–V, which had similar operating conditions with a few notable exceptions: At the end of the SK I phase (1996–2001), an accident[2] resulted in the loss of roughly half of the experiment's PMTs. During the SK II phase (2002–2005), the remaining PMTs were rearranged to provide uniform but reduced (19%) photocoverage. New PMTs were installed to restore photocoverage to original conditions starting with the SK III phase (2006–2008). In 2008, the experiment's electronics were upgraded [18], marking the start of the SK IV phase (2008–2018). The SK IV electronics upgrade extended the window of hit times recorded following neutrino-like events, which improved the efficiency for detecting decay electrons and enabled the detection of the 2.2 MeV gamma emission following neutron captures on hydrogen [19].

During 2018, the SK detector was drained to conduct work in preparation of loading gadolinium sulfate, a compound with a high neutron capture cross section, into the detector's water. The work comprised of installing a new water circulation system capable of continuously purifying gadolinium sulfate, sealing the welding joints of the tank walls to repair and prevent leaks, and replacing several hundred PMTs that had failed during the SK III and SK IV phases. The subsequent SK V (2019–2020) phase resumed data-taking with pure water and reaffirmed the detector's stability and performance after the refurbishment work. In July 2020, gadolinium was dissolved into the detector's water for the first time [20], marking the start of the SK Gd phase. This work includes data from the pure-water SK I–V phases only. Future analyses using data from the SK Gd phase will feature enhanced neutron-tagging efficiency due to the high-neutron-capture cross section of the gadolinium and its subsequent 8 MeV γ cascade. The operating conditions of the SK phases are summarized in Table II.

The SK detector observes Cherenkov light from charged particles with sufficient momentum produced following neutrino interactions. The light projected onto the PMT-lined walls of the detector forms ring patterns of hit PMTs. The ring patterns are reconstructed using the APFIT [21] algorithm: The timing information of hits establishes an event vertex, and a fit considering the spatial distribution and observed charges of hit PMTs determines the particle's direction, momentum, and particle type. APFIT separates rings into e-like and μ-like: Electrons and photons tend to scatter and produce electromagnetic showers, resulting in many overlapping rings which appear as a single ring with blurred edges. Heavier particles such as muons and charged pions do not create showers, and therefore have sharp ring

---

[2] A single PMT imploded during refilling of the detector, creating a shockwave and chain reaction, destroying additional PMTs. Acrylic covers were mounted to all the PMTs to prevent similar accidents in the future.

TABLE II. Super-Kamiokande data-taking phases. An electronics upgrade at the start of SK IV enabled neutron tagging on hydrogen (H), utilized in the SK IV and SK V phases. During 2020, gadolinium (Gd) was added to the detector's water to increase the neutron-tagging efficiency. At the time of this writing, SK Gd is ongoing, and data from the SK Gd phase are not included in this analysis.

Phase	Dates	Live time (Days)	Photo-coverage (%)	Neutron tagging
SK I	1996–2001	1489.2	40	…
SK II	2002–2005	798.6	19	…
SK III	2006–2008	518.1	40	…
SK IV	2008–2018	3244.4	40	H
SK V	2019–2020	461.0	40	H
SK Gd	2020–Present	…	40	H + Gd

edges. Higher-momentum particles produce more light, so the charge contained within the ring provides an estimate of the particle's momentum. Figure 2 shows an example of the Cherenkov light patterns observed in SK following a neutrino candidate interaction, and their fitted properties. The event contains multiple ring patterns, each corresponding to a different particle.

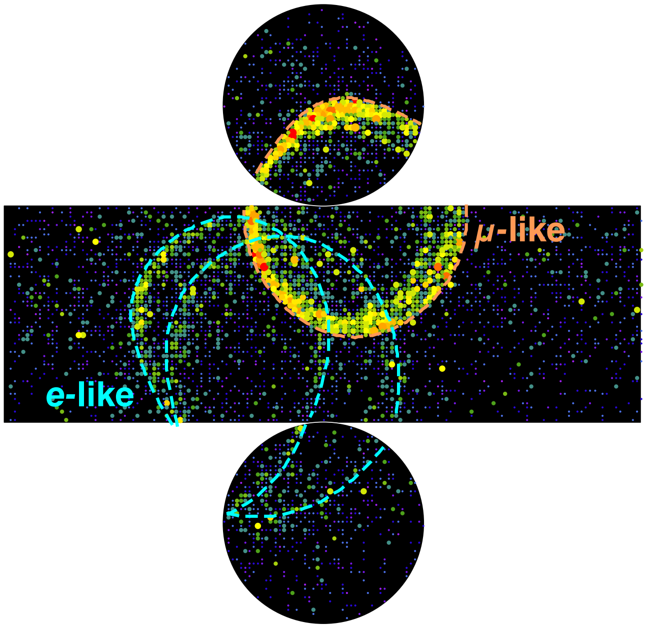

FIG. 2. Event display of a multi-ring atmospheric neutrino cadidate event in SK V data. Hit ID PMTs are displayed on an unrolled view of the cylindrical detector, with the color and radius of each hit PMT corresponding to the detected charge. The reconstruction algorithm APFIT identifies three Cherenkov rings, indicated by dashed outlines: one bright μ-like ring, with $p_\mu \approx 1010\ \mathrm{MeV}/c$, and two fainter e-like rings, each with $p_e \approx 320\ \mathrm{MeV}/c$.

In addition to Cherenkov rings, SK identifies electrons from muon decays. Decay electrons are found by scanning for time-clustered hits following a primary neutrino interaction trigger. A hit-time-based fitter estimates the decay electron vertex for each candidate hit cluster, and candidates are accepted if there are 50 or more hits within a 50 ns time window. The overall decay electron tagging efficiency is estimated to be 96% for μ^+ and 80% for μ^- in the SK IV and SK V periods. The reduced efficiency for μ^- is due to μ^- capture in the water, in which no decay electron is produced.

Neutrons in the SK detector are captured on hydrogen, producing deuterium in an excited state. The decay of the excited deuterium produces a 2.2 MeV γ, which results in a few time-coincident and spatially clustered PMT hits. These γ emissions from neutron captures are identified using a two-step process. In the first step, a sliding 10 ns hit-time window finds candidate neutron captures from clusters of 7–50 hits with fewer than 200 hits in a surrounding 200 ns window. The lower bound of the hit range suppresses spurious coincidences from noise, while the upper bound avoids tagging decay electrons. In the second step, variables which quantify the isotropy, likelihood of single-vertex origin, and the time spread of the hits are calculated for each candidate cluster. A neural network classifies candidates as either signal or background based on these variables. When applied to SK IV–V atmospheric neutrino MC events, the neural network has an average neutron-tagging efficiency for neutron capture on hydrogen of 26% with a background rate of 0.016 false neutrons per event. The uncertainty on the neutron-tagging efficiency is evaluated using an americium-beryllium (AmBe) source embedded in a scintillating box placed at various locations throughout the detector, and is estimated to be 9%. A detailed description of the neutron-tagging algorithm and its development may be found in Ref. [22].

In the SK detector, the charges of particles—and therefore neutrino and antineutrino interactions—cannot be differentiated on an event-by-event basis. However, statistical separation is possible. For example, in the process $\bar{\nu}_\mu + p \to p + \mu^+ + \pi^-$, in which an antineutrino interacts with a proton, the outgoing negatively charged pion is more likely to be captured by an ^{16}O nucleus before decaying than is a positively charged pion produced in the equivalent ν_μ interaction. Captured pions do not produce decay electrons, so requiring one or more decay electrons preferentially selects more neutrino than antineutrino events for this process. The statistical separation can be further improved by also considering the number of neutrons, which will be described in Sec. II B 2.

A. Calibration

Calibration ensures an accurate and consistent response of the detector to particle interactions. Calibration studies

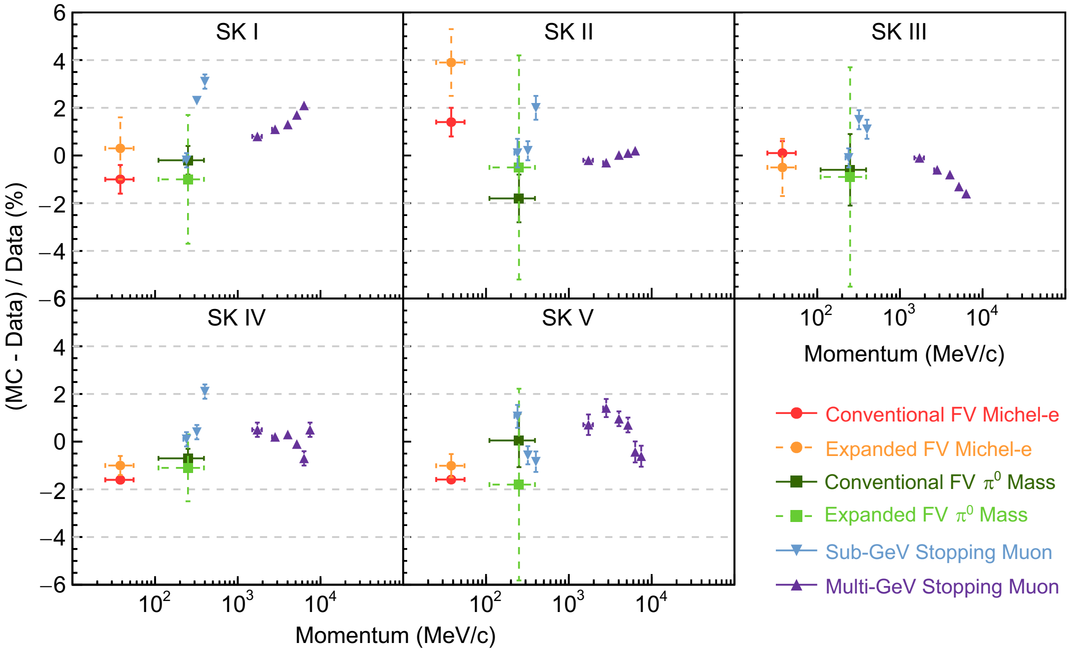

FIG. 3. Performance of energy reconstruction for various sources across all SK periods. Solid points indicate measurements made within the conventional fiducial volume (vertex is greater than 200 cm from the detector walls), while dashed points correspond to measurements in the additional fiducial volume (vertex is between 100 cm and 200 cm from the detector walls). Michel-*e* refers to the stopping muon decay electron spectrum calibration.

based on the detector geometry, PMT responses, and properties of the SK water are documented in Ref. [16]. We assess APFIT's energy determination using calibration sources at multiple energies, which span as much of the atmospheric neutrino energy spectrum as possible. Cosmic ray muons which stop within the detector and produce a decay electron provide a way to measure photoproduction as a function of the muon's track length. The track length of these muons is determined by their ID entrance point and decay electron vertex. The expected momentum of each muon, assuming minimum ionization along the track length, may be compared to the fitted Cherenkov ring momentum. The energy spectrum of decay electrons from these muons also provides a low-energy calibration source. We use the momenta of the two e-like rings from neutral pion decay, $\pi^0 \to \gamma\gamma$, which add to form an invariant mass distribution of neutral pion events, as a third calibration source.

Figure 3 shows the difference between data and Monte Carlo (MC) for the different calibration sources during each SK phase. In this analysis, the decay electron and π^0 mass measurements were also performed separately using events with vertices greater than 200 cm (conventional fiducial volume) and between 100 cm and 200 cm (additional fiducial volume; see Sec. II B 4) from the detector walls. The largest difference, 4%, is observed for the decay electron calibration events in the additional fiducial volume region during the SK II phase.

B. Neutrino sample selection

Neutrino events at SK are broadly categorized as fully contained (FC), partially contained (PC), or upward-going muons (Up-μ). FC and PC events have a reconstructed event vertex within the ID and are differentiated based on the number of hits detected in the OD: FC events have minimal OD activity, while PC events have OD activity following the primary event trigger. Up-μ events are neutrino interactions within the rock below the SK tank or in the OD water which produce muons traveling upward. Figure 4 shows the average number of FC, PC, and Up-μ events observed per day during the SK I–V phases. The average event rates for each category are consistent across all phases within statistical uncertainties.

We separate neutrino candidate interactions from each category into analysis samples to enhance the different oscillation signals present in the atmospheric neutrino data. The data taken during the SK IV and SK V periods, 3705 days, or 57% of the total SK I–V exposure, uses the observed number of neutron captures on hydrogen as an additional classification handle to enhance the purity of neutrino and antineutrino samples.

1. Analysis samples

Fully contained events span the energy range of 100 MeV to 100 GeV and are a mixture of charged-current (CC) and neutral-current (NC) neutrino interactions of all flavors. Because the normal and inverted neutrino mass

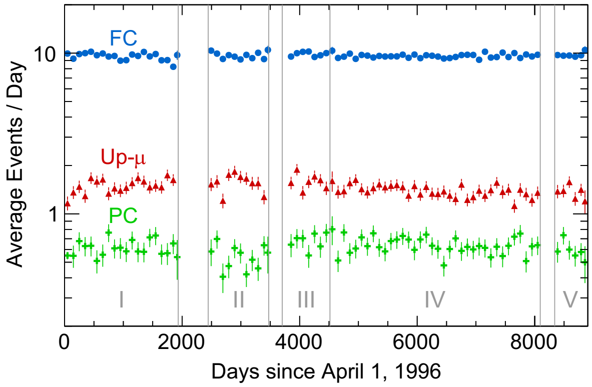

FIG. 4. Average event rates for the primary SK neutrino samples, fully contained (FC), partially contained (PC), and upward-going muons (Up-μ). Error bars are statistical. The five pure-water data-taking phases, SK I–V, are labeled. The FC event rates include events in the additional FV volume region; see Sec. II B 4.

ordering scenarios predict an enhancement to the number of either $\nu_\mu \rightarrow \nu_e$ or $\bar{\nu}_\mu \rightarrow \bar{\nu}_e$ events, and SK cannot distinguish the sign of neutrino interactions on an event-by-event basis, the FC sample definitions are designed to increase the statistical purity of ν_e and $\bar{\nu}_e$ events.

Fully contained events with a single Cherenkov ring are first separated by the ring's particle identification (PID) score, either e-like or μ-like. Events are further divided based on the visible energy E_{vis} into sub-GeV, $E_{\text{vis}} < 1330$ MeV, and multi-GeV, $E_{\text{vis}} > 1330$ MeV. Next, events are separated by the number of decay electrons. For sub-GeV events, we use the number of decay electrons to separate events by likely interaction processes. Samples enhanced with quasielastic interactions are formed by requiring no decay electrons for e-like events and either zero or one decay electron for μ-like events. Sub-GeV e-like and μ-like events with one or more, or two or more decay electrons, respectively, are separated into additional samples enhanced in interaction processes which produce a pion below Cherenkov threshold. For multi-GeV events, the number of decay electrons, either zero, or one or more, is used to separate e-like events into antineutrino- and neutrino-enhanced samples. Fully contained single-ring events in the SK IV and SK V phases have been revised in this analysis to additionally incorporate the number of tagged neutrons and are discussed in Sec. II B 2.

Multi-ring events can contain mixtures of e-like and μ-like rings, making the neutrino flavor ambiguous. However, multi-ring events also provide extra information which is useful for separating ν_e events from $\bar{\nu}_e$ events. For multi-GeV multi-ring events, we use a boosted decision tree (BDT) to classify these events as ν_e-like, $\bar{\nu}_e$-like, μ-like, or "other." The "other" sample primarily selects NC events. More details on the BDT are presented in Sec. II B 3.

Sub-GeV multi-ring events are not included in the analysis due to their poor direction resolution and consequently minimal sensitivity to oscillation effects, with two exceptions: First, multi-ring events with $E_{\text{vis}} > 600$ MeV, where the most energetic ring is μ-like and has a reconstructed momentum of at least 600 MeV$/c$, are included in the multi-ring μ-like sample. Second, FC NC interactions which produce a π^0 are an oscillation-insensitive background to the other samples, but they are included in the analysis to constrain NC interactions. These neutral-current π^0 events are identified from sub-GeV events using a dedicated fitter which assumes there are two rings present, regardless of the number of reconstructed rings. Events are classified as π^0-like based on the likelihood that the two fitted rings originate from a π^0 decay. Events which are classified as π^0-like are separated into two samples based on the number of reconstructed rings without the two-ring assumption, either one or two.

Partially contained events have typical energies between 1 GeV and 1 TeV, and they are nearly all ν_μ CC interactions, as the muon produced in the interaction often exits the ID. The muon momentum in PC events can only be estimated using the portion of the track within the detector. Partially contained events which exit the ID and stop within the OD, determined by comparing the amount of light in the OD to simulated PC events, are classified as stopping, while PC events that completely exit the detector are classified as through-going.

Upward-going muon events are the highest-energy events, up to ~10 TeV, observed at SK and are classified into three samples: "stopping" if the muon stops within the ID, and otherwise "showering" or "nonshowering," depending on whether or not the exiting muon's charge deposition is consistent with radiative losses. The Earth shields the Up-μ sample from cosmic ray backgrounds from below the horizon. However, upward-scattered muons from downward-going cosmic rays are an irreducible background near the horizon. We estimate the background rate in each Up-μ sample at the horizon by comparing the cosmic muon rate at the azimuthal directions with the smallest and largest mountain overburdens. The estimated number of background events is subtracted from the number of Up-μ data events with reconstructed directions near the horizon. The estimated Up-μ background rate is approximately 2%–3%.

The event classification outlined in this section corresponds to 19 distinct analysis samples. There are eight FC CC-enhanced single-ring samples which are used for data collected during the SK I–III phases, while the remaining 11 FC multi-ring, NC π^0, PC, and Up-μ samples are used for data taken during all phases. The data and MC counts for the 19 standard analysis samples are presented in Fig. 5 as a function of reconstructed lepton momentum or zenith angle.

2. SK IV–V neutron-tagged samples

This analysis modifies the FC single-ring event selection during the SK IV and SK V phases based on the number of

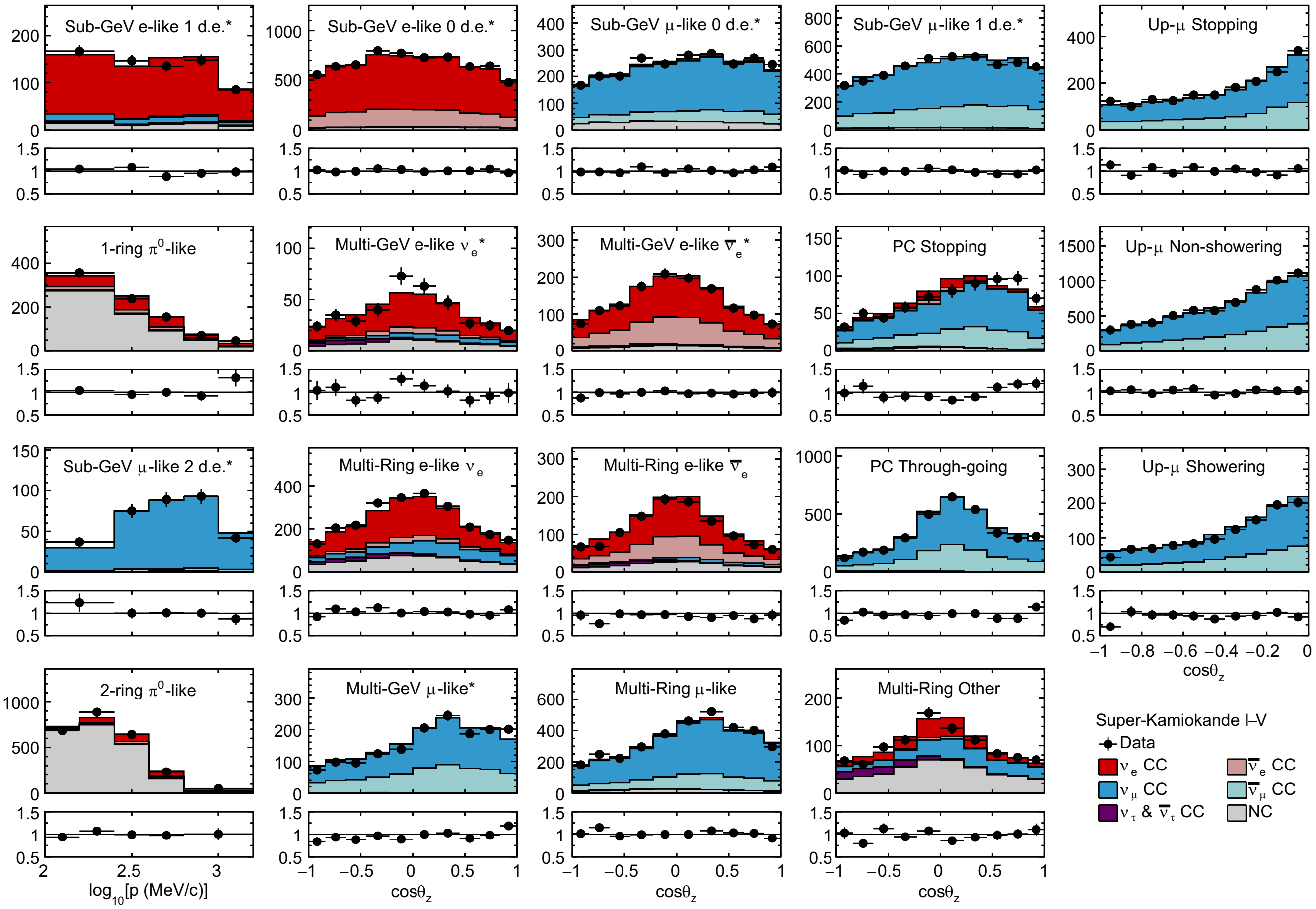

FIG. 5. Zenith angle or momentum distributions for the 19 analysis samples without neutron tagging. The first column shows the momentum bins for samples which are not also binned by zenith angle, while the second through fifth columns show the 1D zenith angle distributions for samples which use 2D momentum and zenith angle binning. The MC distributions are shown at the best-fit point in the normal ordering, cf. Table IV, with best-fit systematic pulls applied. Different colors in the MC histograms correspond to the true neutrino flavors present in each sample. Panels beneath each distribution show the data-MC ratio, and all error bars are statistical. FC (non-PC and non-Up-μ) sub-GeV and multi-GeV single-ring samples, marked with an asterisk (*), contain events from only SK I–III, while the corresponding events from SK IV–V are separated into samples using tagged neutron information, shown in Fig. 6.

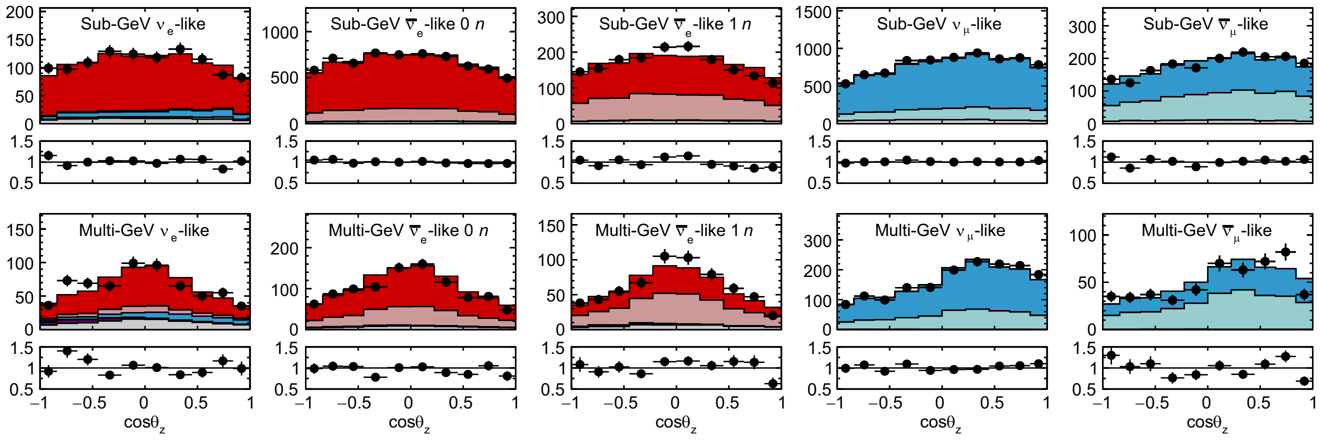

FIG. 6. Zenith angle distributions for the SK IV and SK V FC sub-GeV and multi-GeV single-ring samples using the number of tagged neutrons. The MC configuration and the meaning of the colors are identical to Fig. 5.

TABLE III. Monte Carlo CC and NC purities by sample and data event counts used in this analysis. Purities and MC counts are shown with oscillation probabilities applied and without the effects of systematic pulls. The "ν_τ CC" column shows the purity of both ν_τ and $\bar{\nu}_\tau$ CC events. The Up-μ data counts are shown after background subtraction.

			MC purity						Events	
Sample	Energy bins	$\cos\theta_z$ bins	ν_e CC	$\bar{\nu}_e$ CC	ν_μ CC	$\bar{\nu}_\mu$ CC	ν_τ CC	NC	MC	Data
Fully contained (FC), single ring, sub-GeV										
SK I–III:										
e-like										
0 decay-e	5 $e^\pm$ momentum	10 in $[-1,1]$	0.733	0.226	0.003	0.001	0.000	0.036	6409.1	6647
1 decay-e	5 $e^\pm$ momentum	single bin	0.796	0.016	0.086	0.020	0.001	0.081	612.0	682
μ-like										
0 decay-e	5 $\mu^\pm$ momentum	10 in $[-1,1]$	0.027	0.008	0.704	0.149	0.001	0.112	2153.9	2419
1 decay-e	5 $\mu^\pm$ momentum	10 in $[-1,1]$	0.001	0.000	0.677	0.291	0.000	0.030	4241.4	4476
2 decay-e	5 $\mu^\pm$ momentum	single bin	0.001	0.000	0.948	0.029	0.001	0.022	330.7	336
SK IV–V:										
ν_e-like	5 $e^\pm$ momentum	10 in $[-1,1]$	0.794	0.016	0.090	0.024	0.001	0.074	943.7	1093
$\bar{\nu}_e$-like 0n	5 $e^\pm$ momentum	10 in $[-1,1]$	0.789	0.175	0.003	0.001	0.000	0.031	5961.8	6669
$\bar{\nu}_e$-like 1n	5 $e^\pm$ momentum	10 in $[-1,1]$	0.582	0.367	0.003	0.002	0.001	0.044	2266.6	1668
ν_μ-like	5 $\mu^\pm$ momentum	10 in $[-1,1]$	0.011	0.003	0.755	0.173	0.000	0.057	6596.0	7879
$\bar{\nu}_\mu$-like	5 $\mu^\pm$ momentum	10 in $[-1,1]$	0.001	0.000	0.533	0.417	0.001	0.049	2150.4	1793
Fully contained (FC), single ring, multi-GeV										
SK I–III:										
ν_e-like	4 $e^\pm$ momentum	10 in $[-1,1]$	0.568	0.086	0.102	0.014	0.039	0.190	359.6	383
$\bar{\nu}_e$-like	4 $e^\pm$ momentum	10 in $[-1,1]$	0.556	0.341	0.013	0.002	0.012	0.075	1359.8	1339
ν_μ-like	2 $\mu^\pm$ momentum	10 in $[-1,1]$	0.002	0.001	0.621	0.371	0.003	0.002	1588.5	1564
SK IV–V:										
ν_e-like	4 $e^\pm$ momentum	10 in $[-1,1]$	0.607	0.087	0.098	0.015	0.033	0.159	584.1	643
$\bar{\nu}_e$-like 0n	4 $e^\pm$ momentum	10 in $[-1,1]$	0.637	0.287	0.008	0.002	0.007	0.058	866.4	986
$\bar{\nu}_e$-like 1n	4 $e^\pm$ momentum	10 in $[-1,1]$	0.435	0.460	0.009	0.002	0.015	0.079	736.1	616
ν_μ-like	2 $\mu^\pm$ momentum	10 in $[-1,1]$	0.002	0.001	0.695	0.297	0.003	0.001	1464.0	1619
$\bar{\nu}_\mu$-like	2 $\mu^\pm$ momentum	10 in $[-1,1]$	0.001	0.000	0.446	0.549	0.004	0.002	593.1	503
SK I–V common samples:										
Fully contained (FC) Sub-GeV NC π^0-like										
Single-ring	5 $e^\pm$ momentum	single bin	0.219	0.064	0.018	0.002	0.001	0.696	748.0	868
Two-ring	5 π^0 momentum	single bin	0.096	0.028	0.015	0.001	0.000	0.860	2095.3	2494
Fully contained (FC) Multi-GeV, multi-ring										
ν_e-like	3 visible energy	10 in $[-1,1]$	0.495	0.066	0.175	0.014	0.035	0.215	2149.7	2411
$\bar{\nu}_e$-like	3 visible energy	10 in $[-1,1]$	0.519	0.260	0.052	0.007	0.025	0.138	1210.0	1131
μ-like	4 visible energy	10 in $[-1,1]$	0.028	0.003	0.713	0.200	0.006	0.050	3257.7	3427
Other	4 visible energy	10 in $[-1,1]$	0.203	0.023	0.257	0.014	0.074	0.429	837.9	982
Partially contained (PC)										
Stopping	2 visible energy	10 in $[-1,1]$	0.089	0.034	0.559	0.262	0.011	0.045	641.6	689
Through-going	4 visible energy	10 in $[-1,1]$	0.006	0.002	0.638	0.341	0.007	0.006	3310.2	3397
Upward-going muons $(Up-\mu)$										
Stopping	3 visible energy	10 in $[-1,0]$	0.008	0.003	0.646	0.340	0.000	0.003	1574.3	1753.8
Nonshowering	single bin	10 in $[-1,0]$	0.002	0.001	0.662	0.334	0.000	0.001	5315.8	6423.9
Showering	single bin	10 in $[-1,0]$	0.001	0.000	0.671	0.327	0.000	0.001	1051.4	1110.6

observed neutron captures on hydrogen. The modification is motivated by the greater average neutron production in antineutrino interactions relative to neutrino interactions: Additional neutrons are expected in antineutrino events from proton-to-neutron ($p \rightarrow n$) conversions in CC processes, $\bar{\nu}_l + p \rightarrow l^+ + n + X$, where l denotes lepton flavor, and also in both CC and NC deep inelastic scattering (DIS) processes due to the larger fraction of energy transferred to the recoiling hadronic system. We have incorporated neutron information into the analysis sample definitions to create ten additional samples, five for sub-GeV events and five for multi-GeV events, as follows:

FC single-ring e-like: Both sub-GeV and multi-GeV events are divided into three samples: Events with one or more decay electron and any number of neutrons are classified as ν_e-like. Events with no decay electrons are considered $\bar{\nu}_e$-like, and they are further separated into two samples based on whether or not there is at least one tagged neutron.

FC single-ring μ-like: Both sub-GeV and multi-GeV events are divided into two subsamples: Events with exactly one decay electron and one or more tagged neutrons are considered $\bar{\nu}_\mu$-like; otherwise, they are considered ν_μ-like.

More details about the neutron-tagging algorithm and the event selection modifications may be found in Refs. [22,23]. Figure 6 shows the data and MC comparisons for the SK IV–V neutron tagged samples. Compared to the equivalent antineutrino samples shown in Fig. 5, the SK IV–V $\bar{\nu}_e$ samples requiring at least one tagged neutron have a higher purity of true $\bar{\nu}_e$ MC events, summarized in Table III.

3. Multi-ring boosted decision tree

Multi-ring events in SK often result from the presence of energetic final-state pions. Charged pions are typically reconstructed as μ-like rings, while neutral pions generate e-like rings from their decays. The mixture of ring flavors in multi-ring events can cause ambiguity when attempting to classify the event by the interacting neutrino's flavor. On the other hand, the additional rings provide extra observable information not available in single-ring events. To classify multi-ring events based on a synthesis of the available information, we consider seven reconstructed quantities [24]. As in the single-ring classification, the primary quantity used to separate μ-like events from e-like events is the PID score of the most energetic ring in the event. To further improve the $e-\mu$ separation, we also consider the maximum distance of any decay electrons from the event vertex, $L_{\mathrm{Decay}e}$. $L_{\mathrm{Decay}e}$ differs between μ-like and e-like events because, while both electron- and muon-neutrino CC interactions may have decay electrons produced from pion decays, the muons produced in muon neutrino CC interactions typically have higher momenta than additional charged pions, and so the muons travel further before decaying. To separate ν_e-like events from $\bar{\nu}_e$-like events, we again consider the number of decay electrons. We also utilize the additional kinematic information present in multi-ring events by comparing the number of rings and two additional variables based on the distribution of ring momenta, the fraction of the momentum carried by the most energetic ring, $p_{\mathrm{Max}}/p_{\mathrm{Tot}}$, and the fraction of momentum transverse to the most energetic ring's direction, $p_{\mathrm{T}}/p_{\mathrm{Tot}}$ These kinematic variables differ between ν_e and $\bar{\nu}_e$ events due to the different angular and momentum dependencies between neutrino and antineutrino cross sections. Finally, we use the visible energy to separate ν_τ events which only occur at higher energies due to the energy threshold of their interactions. Based on these variables, we create four analysis samples for multi-ring events: CC ν_e-like, CC $\bar{\nu}_e$-like, CC μ-like (both ν_μ and $\bar{\nu}_\mu$), and "other." The "other" category is intended to separate NC and ν_τ interactions from the CC-enhanced categories.

Previous versions of this analysis used a likelihood-based classification algorithm with the seven reconstruction quantities as inputs [24]. This analysis replaces the likelihood-based selection with a boosted decision tree (BDT) utilizing the same set of variables as in the likelihood-based classification [25]. The BDT is trained on labeled true multi-ring MC events equivalent to a 430-year exposure and validated on MC events equivalent to a 70-year exposure for each SK phase. We optimize the BDT for sensitivity to the neutrino mass ordering by weighting the training events. Adjusting the weights of CC ν_e and $\bar{\nu}_e$ training events relative to CC ν_μ and "other" events changes the expected signal purities obtained from the BDT selection, which in turn affects the expected mass-ordering sensitivity. Compared to the likelihood-based classification, we find that the optimized BDT increases the efficiencies of correctly classifying true CC events from 35% to 55% for ν_e, from 58% to 65% for $\bar{\nu}_e$, and from 74% to 81% for ν_μ, while decreasing the efficiency for correctly classifying NC events from 57% to 31%. The purity of true ν_e CC events in the ν_e-like sample decreases from 56% to 50%, while the purities of correctly classified CC events in the $\bar{\nu}_e$-like and ν_μ-like samples (26% and 91%, respectively) are unchanged, and the purity of correctly classified NC events in the "other" sample increases from 30% to 43%. Accounting for differences in exposure, the increased efficiencies in the CC samples result in proportionally larger statistics in the CC ν_e-like, $\bar{\nu}_e$-like, and ν_μ-like multi-ring samples and decreased statistics in the "other" sample compared to the previous analysis.

Figure 7 shows the distributions of the BDT input variables from MC events. The largest differences between electron- and muon-flavor neutrino interactions are in the PID of the most energetic ring and the maximum distance travelled by decay electrons, $L_{\mathrm{Decay}e}$. Electron neutrino and antineutrino multi-ring events differ in the expected number of decay electrons, the number of rings, and in the fractional momentum variables $p_{\mathrm{Max}}/p_{\mathrm{Tot}}$ and $p_{\mathrm{T}}/p_{\mathrm{Tot}}$ Figure 8 demonstrates the ν_e and $\bar{\nu}_e$ separation performance of the BDT in the SK IV–V phases. Neutron information from the SK IV–V phases was also considered as an input variable to the BDT, but it was found to only result in a marginal improvement to ν_e-$\bar{\nu}_e$ separation while introducing a large amount of systematic uncertainty.

4. Expanded fiducial volume

Previous SK analyses used a 22.5 kiloton fiducial volume for FC events defined by requiring that the reconstructed event vertex be at least 200 cm away from the ID walls (conventional fiducial volume). This analysis includes events reconstructed within the 4.7 kiloton region

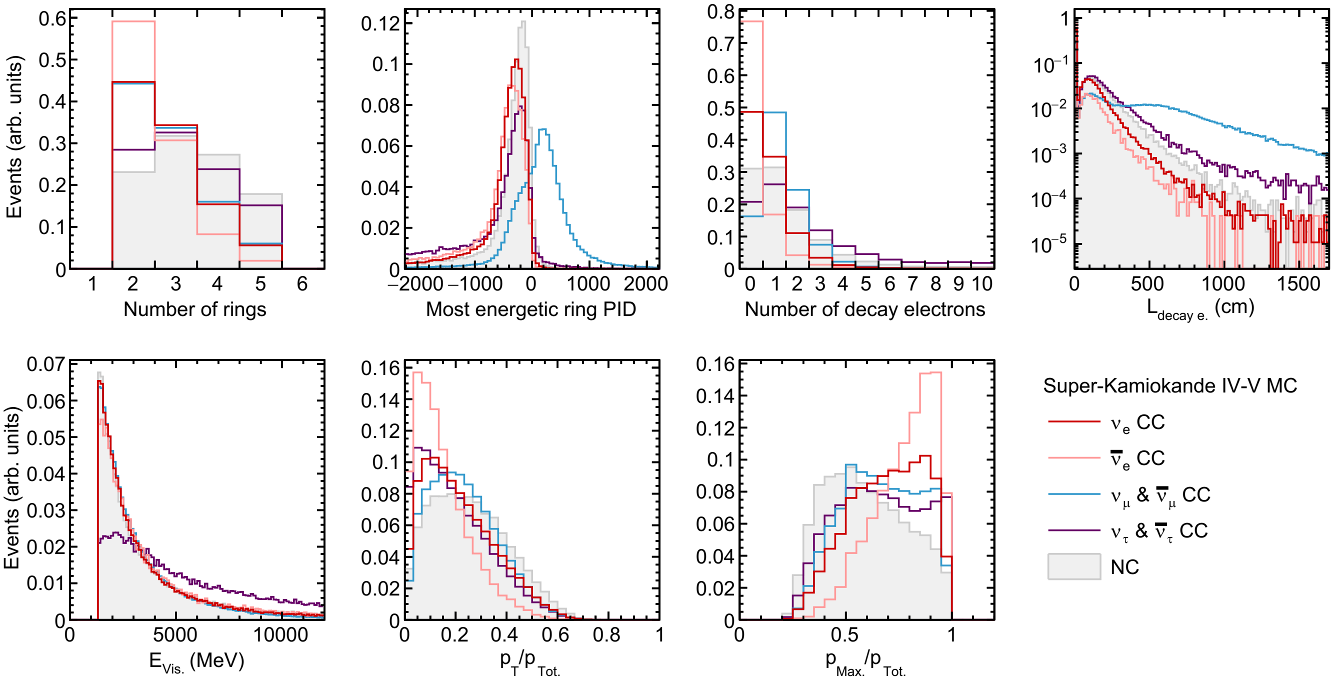

FIG. 7. Monte Carlo distributions of input variables for the FC multi-GeV, multi-ring BDT. Distributions are area-normalized. $L_{\mathrm{Decay\,e}}$ is the maximum distance of any decay electron from the event's primary vertex. p_{T} is the momentum transverse to the most energetic ring, $p_{\mathrm{Max.}}$ is the momentum of the most energetic ring, and p_{Tot} is the sum of the momenta from all reconstructed rings.

100–200 cm from the ID walls (additional fiducial volume) for all SK phases, representing a 20% increase in exposure. To include events in the additional fiducial volume region, both the reconstruction algorithms and background estimations required reevaluation [26]. In 2018, the pre-tabulated expected charge distributions, which are the basis of the ring counting and PID likelihoods used in APFIT, were recomputed as a function of a particle's distance to the nearest detector wall. These new charge tables encode the reduced number of hits and increased angular dependence expected from events near the detector walls. Adopting the updated charge tables reduced the e-μ misidentification of single-ring events in the additional region by up to 35%.

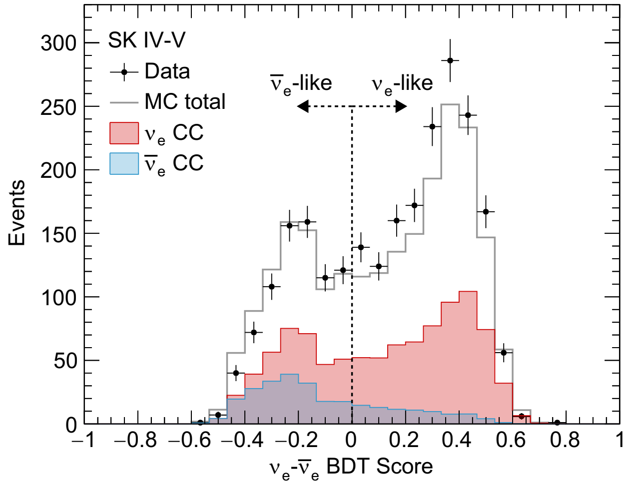

FIG. 8. Data and MC distributions of the multi-ring BDT classifier scores for multi-ring ν_e and $\bar{\nu}_e$ events. The BDT makes a final classification decision for each event based on the class with the highest score: Negative values correspond to $\bar{\nu}_e$-like events, and positive values correspond to ν_e-like events. Distributions are shown for the SK IV–V phases, including events in the expanded fiducial volume region. MC events are shown with oscillations applied, and without the effect of any fitted systematic uncertainty parameters. The "MC total" distribution includes contributions from true ν_μ, ν_τ, and NC events.

Cosmic muons with vertices misreconstructed inside the fiducial volume also become more prevalent closer to the detector walls. To estimate the size of these backgrounds, events in the additional fiducial volume region were eye-scanned by experts. A slightly higher background rate of 0.5%, compared to 0.1% in the conventional fiducial volume, was found. The increased background rate in the additional fiducial volume is acceptable, although the background rate rises quickly for events with reconstructed vertices less than 100 cm from the detector walls, prohibiting further expansion.

We note that Ref. [26] included events from the additional fiducial volume region in the context of a proton decay search which was primarily concerned with sub-GeV atmospheric neutrino backgrounds. In contrast, this oscillation analysis includes both sub-GeV and multi-GeV atmospheric neutrino events. Additional studies to those presented in Ref. [26] were needed to confirm the performance of the reconstruction algorithms for multi-GeV events in the additional fiducial volume region. We studied the reconstructed momentum and direction biases and

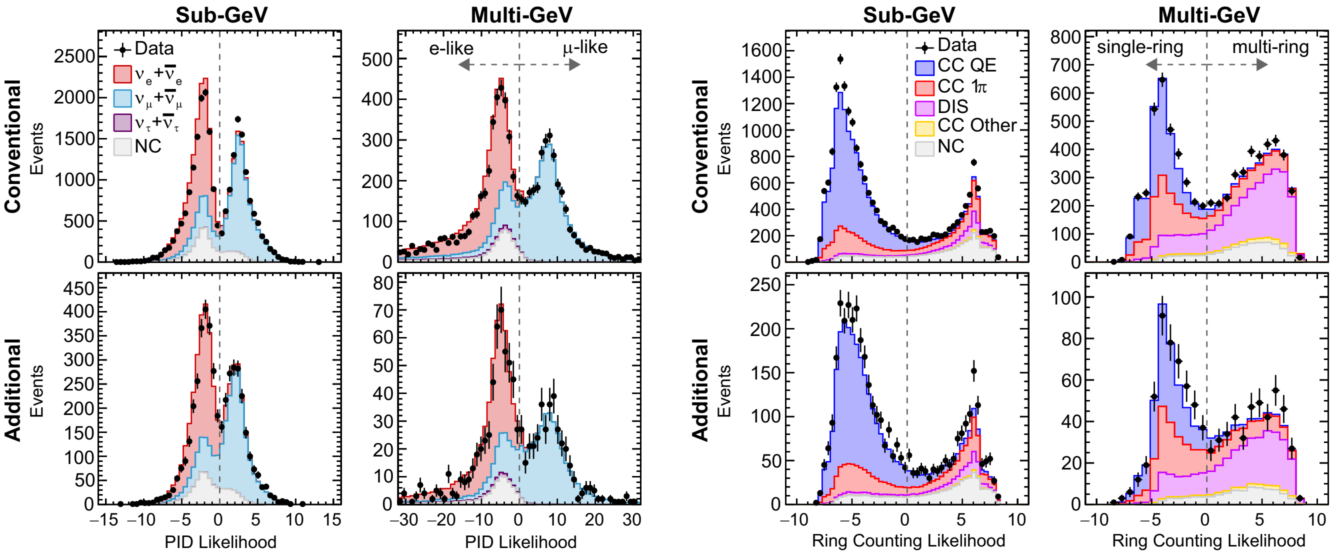

FIG. 9. SK IV–V data and MC distributions of the likelihood variables used to classify events into the different analysis samples. The top row shows events in the conventional fiducial volume region, while the bottom row shows events in the additional fiducial volume region. The first and third columns show sub-GeV events, and the second and fourth columns show multi-GeV events. The left four panels show the PID likelihood for the most energetic ring in each event: Negative values indicate the ring is e-like, while positive values indicate the ring is μ-like. The right four panels show the ring-counting likelihood: Negative values indicate the event has a single ring, while positive values indicate the event has multiple rings. In these panels, the "CC QE" histograms include both 1p1h and 2p2h processes, and "CC Other" refers to single, nonpion hadron production. All MC distributions are calculated assuming neutrino oscillations and without the effect of any systematic uncertainties.

resolutions using MC events, and we confirmed that these quantities were similar between events in the conventional and additional fiducial volume regions. We also studied the data versus MC agreement between the ring PID and ring-counting likelihoods for events in the additional fiducial volume region, as shown in Fig. 9. The figure compares the data and MC distributions for sub-GeV and multi-GeV events in both fiducial volume regions. The level of agreement in the likelihood distributions using the updated reconstruction algorithms is found to be equivalent between events in the conventional and expanded fiducial volume regions at both sub-GeV and multi-GeV energies.

This analysis is the first SK atmospheric neutrino oscillation analysis to include FC events from the additional fiducial volume region, resulting in a total fiducial volume of 27.2 kilotons for all SK phases. The total exposure for FC events in this analysis is 484.2 kiloton-years, a 48% increase over the previous published analysis.

III. SIMULATION

We produce simulated Monte Carlo (MC) events to provide a prediction of atmospheric neutrino data. The SK MC consists of simulated neutrino interactions generated according to the flux model of Honda *et al.* [27] and the cross-section models of the NEUT simulation software [28,29]. NEUT also propagates intermediate particles within the nuclear medium and produces the final-state particles which exit the nucleus. These final-state particles are stepped through a GEANT3-based [30] simulation of the SK detector which models particle propagation in the detector water, Cherenkov radiation emission, and the detection of Cherenkov radiation by PMTs [16]. The SK detector simulation also implements a data-driven model of PMT electronics, dark noise, and disabled PMTs.

A. Neutrino interaction model

Because atmospheric neutrinos span several orders of magnitude in energy, multiple interaction processes are relevant across the different SK neutrino samples. Fully contained events, which are the lowest-energy atmospheric neutrinos in this analysis, have leading contributions from charged-current quasielastic (CCQE) and single-pion production processes. Partially contained and Up-μ events consist of higher-energy neutrinos where deep inelastic scattering (DIS) becomes dominant. The contribution to the event rate from each cross section process is shown in Fig. 10.

This analysis uses NEUT version 5.4.0 [29] for the nominal neutrino interaction models, which is an update from version 5.3.6 used in the previous analysis. Notable changes in this version include the replacement of the nominal one-particle-one-hole (1p1h) model, responsible for the CCQE and NCQE processes, from the Smith and Moniz relativistic Fermi gas (RFG) model [32] to the local Fermi gas (LFG) model by Nieves *et al.* [33]. The nominal value of the axial mass parameter M_A^{QE} was decreased from

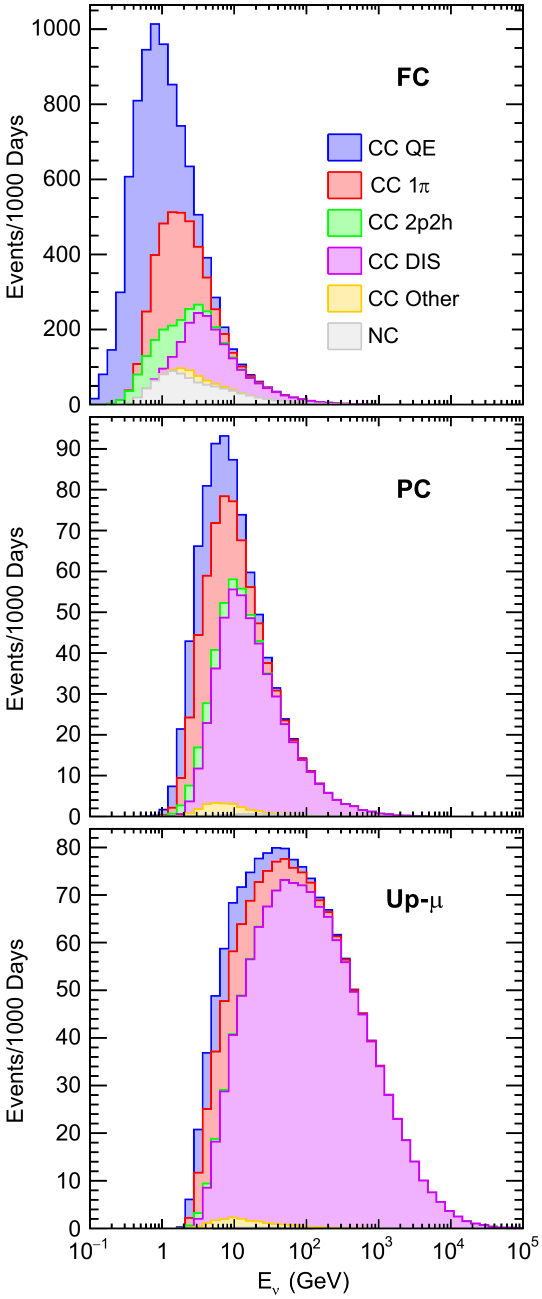

FIG. 10. Simulated neutrino energy spectra by interaction modes for the different SK event categories: fully contained (FC), partially contained (PC), and upward-going muon (Up-μ). The simulated event rates are for an oscillated MC, with oscillation parameters set to the Particle Data Group best-fit values [31], except for δ_{CP}, which is set to 0. "CC Other" modes refer to the production of single, nonpion hadrons.

1.21 GeV$/c^2$ to 1.05 GeV$/c^2$. This change results in an overall decrease of CCQE events in the nominal MC by $\sim$20%, although the previous M_A^{QE} value is still within the 1σ uncertainty; see Sec. IV B. The LFG model also includes a correction to the cross section at low four-momentum (q^2) transfers due to weak charge screening calculated via the random phase approximation (RPA) technique [34]. The BBBA05 [35] vector form factors are used in the nominal 1p1h model, which is unchanged from the previous analysis.

NEUT implements the Rein-Sehgal resonant single-pion production model [36], which is unchanged from the previous analysis. The coherent pion production cross-section calculation, which was previously based on the Rein-Sehgal model, has been updated to use the Berger-Sehgal model [37] for neutrino events with $E_\nu < 10$ GeV. This was done to improve the agreement in total cross section and angular distribution of the outgoing pion with recent scattering experiments [38].

Deep inelastic scattering cross sections in NEUT are calculated using the GRV98 parton distribution functions (PDFs) [39], with corrections to the low-q^2 regime from Bodek and Yang [40]. NEUT simulates the production of multiple hadrons using two separate models, selected based on the invariant mass of the hadronic system, W. For $W < 2$ GeV, a custom multi-pion generator is used, while for $W > 2$ GeV, NEUT uses PYTHIA v5.72 [41]. The DIS hadron production models are only used to produce final states with multiple hadrons to avoid overlap with the single-hadron models.

Final-state interactions (FSIs) are processes which modify particles exiting the nucleus due to intranuclear effects. Secondary interactions (SIs) are equivalent processes which occur in the detector medium instead of within the nucleus. NEUT implements four FSI + SI processes: quasielastic scattering, charge exchange, pion absorption, and hadron production. Six parameters adjust the probabilities of these processes. NEUT 5.4.0 updated the default values of these parameters [42], which increased the pion absorption probability by 27%, and decreased the probability of charge exchange for pions with momentum < 400 MeV$/c$ by 30% compared to version 5.3.6.

The cross section for the two-particle-two-hole (2p2h) process, in which no pions are produced but a pair of nucleons is ejected from the nucleus, is calculated using the Valencia model of Nieves *et al.* [43]. This is unchanged from the previous version of NEUT.

IV. ATMOSPHERIC NEUTRINO OSCILLATION ANALYSIS

Atmospheric neutrino data are analyzed via the fit of binned MC counts to data. We bin atmospheric neutrino MC and data events using two-dimensional bins of reconstructed cosine zenith angle and momentum. The bin definitions for the 29 samples used in this analysis are listed in Table III. The zenith angle bin definitions were updated for this analysis and are discussed in Sec. IV A.

Systematic uncertainties are incorporated in the analysis as additional nuisance parameters which modify the nominal MC prediction in the fit. We estimate the effect of each systematic uncertainty by quantifying the change induced in each analysis bin due to $+1\sigma$ and -1σ deviations from its nominal value. The systematic uncertainties considered in this analysis are described in Sec. IV B.

A. Zenith angle binning

In the previous analysis, FC and PC events were binned into ten evenly spaced cosine zenith angle bins on the interval $[-1, 1]$. This separated the expected oscillation resonance region across two bins, reducing the signal-to-background ratio in samples sensitive to the neutrino mass ordering. In this analysis, the zenith angle bins for FC and PC events have been updated to more precisely cover the resonance region, demonstrated in Fig. 11. The updated bins are defined by the edges −1, −0.839, −0.644, −0.448, −0.224, 0, 0.224, 0.448, 0.644, 0.839, and 1. With the present statistics, adopting the updated bins results in a negligible effect on the expected sensitivity of this analysis to the mass ordering. However, the updated bins reduce the ambiguity as to whether or not events in the signal region occur in the expected zenith angle range or slightly outside of it.

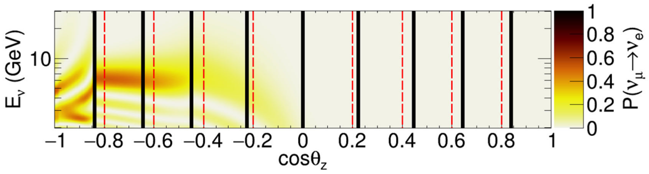

FIG. 11. Updated zenith angle bin edges for this analysis (black, solid lines) compared to equally spaced bins (red, dashed lines). The updated bin edges are symmetric about zero and align with the matter-enhanced $\nu_\mu \to \nu_e$ resonance regions present assuming the PREM. The oscillation probabilities and corresponding color scale are the same as in Fig. 1 for neutrinos in the normal ordering.

B. Systematic uncertainties

The analysis includes 193 independent systematic uncertainty sources: 48 describe atmospheric neutrino flux and cross section effects common to all phases, and the remaining 29×5 describe reconstruction efficiencies which are separately estimated for each data-taking phase. Additional details on the formulation of the systematic uncertainties may be found in Ref. [44].

1. Flux and cross-section uncertainties

The atmospheric neutrino flux uncertainties in this analysis are unchanged from the previous analysis [5]. Two energy-dependent uncertainties scale the normalization of the flux above and below 1 GeV. Additionally, there are three energy-dependent uncertainties which modify the ratios of muon-to-electron, electron-to-antielectron, and muon-to-antimuon flavor neutrinos present in the atmospheric neutrino flux. An uncertainty based on the ratio of the Honda flux calculation with a modified kaon-to-pion ratio over the nominal model is also included [45]. There are two additional uncertainties which allow modifications to the flux shape. The first modifies the ratio between upward-going ($\cos\theta_z < 0$) and downward-going ($\cos\theta_z > 0$) events, while the second modifies the ratio between vertical ($\cos\theta_z > 0.9$) events and horizontal ($0 < \cos\theta_z < 0.1$) events. The effect size of the shape uncertainties is separately estimated for each neutrino flavor and for sub-GeV and multi-GeV events.

The effects of uncertainties on parameters in the CCQE and single-pion cross-section models are computed by reweighting MC events by the ratio of the double-differential cross section after $+1\sigma$ and -1σ changes in each parameter. For CCQE events, M_A^{QE} is taken to be $(1.05 \pm 0.16)\ \mathrm{GeV}/c^2$. There are three parameters which control the single-pion production cross section in the Rein-Sehgal model: the axial mass, $M_A^{\mathrm{Res}} = (0.95 \pm 0.15)\ \mathrm{GeV}/c^2$; the axial form factor coefficient, $C_A^5 = 1.01 \pm 0.12$; and the isospin-$\frac{1}{2}$ background contribution scaling parameter, $I_{\frac{1}{2}} = 1.30 \pm 0.20$.

In addition to the M_A^{QE} uncertainty, we place additional uncertainty on CCQE events due to differences between the LFG and RFG models. There are five uncertainties where the 1σ effect is computed by forming ratios between the predictions of the two models: the absolute event rate (both sub-GeV and multi-GeV), the shape of the E_ν dependence, and the ratios of ν_μ/ν_e and $\bar{\nu}_\mu/\bar{\nu}_e$. These uncertainties are computed as a function of neutrino energy. The uncertainty on the 2p2h contribution to CCQE interactions is set to 100% due to a lack of direct measurements, and it is unchanged from the previous analysis.

An uncertainty on FSIs and SIs is implemented by recomputing the final states for MC events using multiple sets of the six NEUT FSI parameters. Each set consists of variations of one or more FSI parameters by their $\pm 1\sigma$ uncertainties as determined by a fit to external pion scattering from Ref. [46]. The set which produces the largest change in classification outcome is taken as a conservative estimate of the FSI + SI uncertainty.

Two neutron-related systematic uncertainties are included in this analysis to account for the dependence on neutron production models in the neutron-based event selection used for SK IV and SK V data. Variations in these systematic uncertainties move events between samples with no tagged neutrons and samples with one or more tagged neutrons. The largest of the two uncertainties originates from measurements of neutron production as a function of transverse momentum by T2K [47]. An additional neutron-related systematic uncertainty accounts for differences in neutron multiplicity predicted by the different neutrino interaction generators NEUT and GENIE [48].

In addition to model parameter uncertainties, we assign a 20% uncertainty on the ratio of NC to CC events and a 25% uncertainty on the tau neutrino CC cross section [49].

The tau neutrino cross section uncertainty was estimated from a comparison between NEUT and the cross section model of Hagiwara *et al.* [50].

2. Reconstruction uncertainties

Ring reconstruction systematic uncertainties include efficiencies of ring-based particle identification (PID), ring counting, and identification of π^0 decays. The estimation of these systematic uncertainties is unchanged from the previous analysis and is performed using a "scale-and-shift" procedure: First, MC events are labeled as either signal or background, where the particular label differs for each systematic uncertainty source. For example, the ring-counting systematic uncertainty estimation considers events with a single charged particle with true momentum sufficient to produce a Cherenkov ring as signal, and events with multiple particles capable of producing rings as background. Similarly, the PID uncertainty estimation considers true e-like events as signal and true μ-like events as background. Once labeled, the signal and background distributions of each reconstruction quantity x (e.g., the ring-counting or PID likelihoods) are scaled and shifted by a linear function, $x' = \beta_0 + \beta_1 x$, and fit to a subset of atmospheric neutrino data. The signal and background distributions have independent β parameters. The fitted β parameters are then fluctuated according to their fitted uncertainties to generate toy datasets with random amounts of signal and background events. The maximum fractional change in signal purity observed in the toy datasets is taken as a conservative estimate of the uncertainty.

The scale-and-shift procedure is used to separately evaluate ring-related systematic uncertainties for events in the conventional and additional fiducial volume regions during each data-taking phase. The ring-counting and PID systematic uncertainties are separately computed for each combination of e-like and μ-like, and sub-GeV and multi-GeV events. As in the previous analysis, the scale-and-shift procedure is used to place an additional uncertainty on the normalization of ν_μ contamination present in the e-like samples, estimated from the fitted fraction of ν_μ events classified as e-like. We also use the scale-and-shift procedure to estimate the uncertainty associated with the multi-ring BDT: Two sources of systematic uncertainty are considered for multi-ring events based on the data-MC agreement in the input distributions used to train the BDT, and in the output BDT scores themselves. The changes in the event rate in each multi-ring sample obtained through fluctuating the input and output distributions according to their fitted uncertainty are taken as the 1σ effects.

As in the previous analysis, this analysis takes the maximum data-MC disagreement between the decay electron, π^0 mass, and stopping muon calibration sources during each SK phase, shown in Fig. 3, as an estimate of the overall energy scale uncertainty. Variations in this uncertainty increase or decrease the reconstructed momenta of all MC events, causing these events to move between momentum bins. The energy scale uncertainty was newly estimated for the SK V phase and is 1.8% in the conventional fiducial volume and 2.0% in the additional fiducial volume.

This analysis introduces a systematic uncertainty for the neutron-tagging efficiency and false detection rate during the SK IV and SK V phases, which is factored into two components: detector conditions and neutron travel distance. The contribution to the uncertainty due to detector conditions was estimated from comparisons between data from an AmBe source [51] and MC events generated with variations in PMT gain, PMT dark rate, and water transparency within the ranges observed during the SK IV–V phases. The neutron travel distance contribution to the uncertainty was estimated from an atmospheric neutrino data-MC comparison of the distance between the primary neutrino event vertex and the reconstructed neutron capture vertex, convolved with the estimated capture efficiency as a function of the distance. The quadrature sum of these effects sets the overall neutron-tagging uncertainty. Similarly to the neutron production uncertainties, variations in the tagging efficiency uncertainty move events between samples requiring no tagged neutrons and samples requiring one or more tagged neutrons.

The systematic uncertainties with the largest effect on the analysis's sensitivity to the neutrino mass ordering are those which can change the ratio of upward-going ($\cos\theta_z < 0$) versus downward-going ($\cos\theta_z > 0$) events in the multi-GeV e-like samples. This is because the mass-ordering signal region occurs in the upward-going bins of these samples, and downward-going neutrino events act as an unoscillated dataset which constrains uncertainties without zenith angle dependence independent of oscillation effects. Figure 12 shows the estimated largest sources of uncertainty which affect the ratio of upward-versus-downward going events in the multi-GeV e-like samples. The largest source of uncertainty is statistics, indicating the mass-ordering sensitivity is statistics-limited. The ν_τ cross-section uncertainty is the next largest: Tau neutrino interactions at SK are almost exclusively upward-going, since they are the result of $\nu_\mu \to \nu_\tau$ oscillations, so there are no downward-going tau neutrino events to constrain the ν_τ cross-section uncertainty. Additionally, tau neutrino interactions tend to be reconstructed as multi-GeV, multi-ring e-like events, which places them in the mass-ordering signal region [52]. In contrast, uncertainties on the overall flux and cross-section normalizations are less important for the mass-ordering analysis, since these modify the predicted number of events independent of zenith angle.

C. Fitting method

This work presents two fits of atmospheric neutrino data: First, we perform an "atmospheric-only" fit which measures $\Delta m^2_{32,31}$, $\sin^2\theta_{23}$, δ_{CP}, $\sin^2\theta_{13}$, and the neutrino

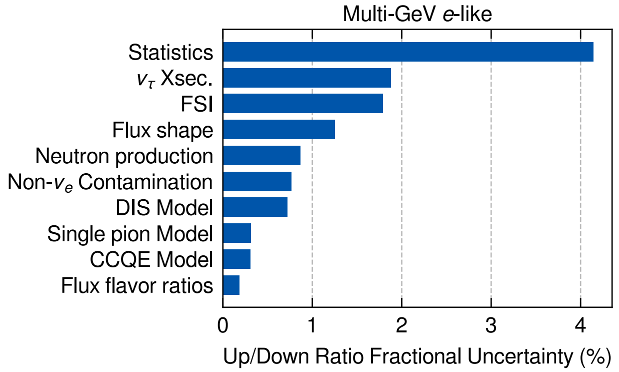

FIG. 12. Estimated fractional uncertainty on the ratio of upward-going, $\cos\theta_z < 0$, versus downward-going, $\cos\theta_z > 0$, events in the multi-GeV *e*-like samples (both single-ring and multi-ring) from statistical and systematic uncertainties. The fractional uncertainties are estimated by randomly fluctuating the nominal MC counts either by Poisson statistics for the "Statistics" entry, or by Gaussian fluctuations of one or more systematic uncertainties. Uncertainties on the up/down ratio in the multi-GeV *e*-like samples have the largest impact on the sensitivity to the neutrino mass ordering.

mass ordering using the SK atmospheric neutrino data with no external constraints. Next, we analyze the same data including a constraint on $\sin^2\theta_{13}$ from reactor neutrino experiments.

In both fits, we evaluate data-MC agreement by computing a χ^2 statistic at each point on a fixed grid of neutrino oscillation parameters, defined for each fit in Table IV. Oscillation probabilities are applied to the MC events using the oscillation parameters at each point in the grid, and systematic uncertainty nuisance parameters are fit to determine the lowest χ^2 value. The best-fit neutrino oscillation parameters are taken to be the grid point with the lowest χ^2 value.

TABLE IV. The oscillation parameter grid definitions used in the three analyses presented in this work. The grids are evenly spaced and include the minimum and maximum values. The grids are the same for both the normal and inverted mass orderings in all analyses. Both analyses treat Δm^2_{21} and $\sin^2\theta_{12}$ as constrained parameters.

Parameter	Minimum	Maximum	Points
SK, Atmospheric only			
$\sin^2\theta_{23}$	0.3	0.775	20
Δm^2_{32} (10^{-3} eV^2)	1.2	3.6	25
δ_{CP} (rad)	$-\pi$	π	21
$\sin^2\theta_{13}$	0	0.075	16
SK, $\sin^2\theta_{13}$ Constrained			
$\sin^2\theta_{23}$	0.3	0.7	35
Δm^2_{32} (10^{-3} eV^2)	1.0	4.9	40
δ_{CP} (rad)	$-\pi$	π	37
$\sin^2\theta_{13}$	0.0220 ± 0.0007		1

The χ^2 statistic is computed via a summation over n bins assuming Poisson statistics, and with systematic uncertainty pull terms, ϵ_i, which have units of σ. Each ϵ_i scales the effect of the ith systematic uncertainty and is included in the χ^2 calculation as an additional penalty term:

$$\chi^2 = \sum_n \left(E_n - O_n + O_n \ln\frac{O_n}{E_n} \right) + \sum_i \epsilon_i^2. \qquad (10)$$

In Eq. (10), n indexes each bin, and O_n are the observed counts in the nth bin. The expected counts E_n are calculated from a nominal MC prediction E_n^0 scaled by the effect of systematic uncertainties. The effect of the ith systematic uncertainty is calculated as ϵ_i times the fractional change induced in the nth bin by a 1σ change, $f_{i,n}$:

$$E_n = E_n^0 \left(1 + \sum_i f_{i,n}\epsilon_i \right). \qquad (11)$$

The constraint $\partial\chi^2/\partial\epsilon_i = 0$ at the minimum χ^2 value yields a system of equations which may be solved to find the configuration of ϵ_i's that produce the smallest χ^2 for a given MC prediction.

D. Mass-ordering sensitivity with neutron tagging

We studied the impact of using neutron captures on hydrogen with a tagging efficiency of 26% on the

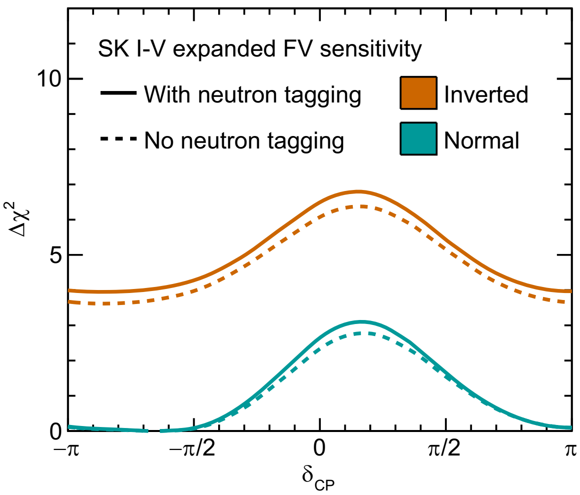

FIG. 13. 1D $\Delta\chi^2$ sensitivity profile of δ_{CP} for the normal and inverted mass-ordering scenarios, with (solid lines) and without (dashed lines) neutron-based event classification for SK IV and SK V data. The sensitivity is computed assuming the true neutrino oscillation parameters are the global best-fit parameters from [31] and the normal mass ordering. The parameters Δm^2_{32}, $\sin^2\theta_{23}$, and δ_{CP} are free parameters in the fit, while the other oscillation parameters are fixed.

sensitivity to the mass ordering. As discussed in Sec. II B 2, tagged neutrons provide an additional handle during event reconstruction which improves the statistical separation of neutrinos and antineutrinos in SK versus only considering the number of decay electrons. This corresponds to an increased purity of correct-sign ν_e and $\bar{\nu}_e$ events in samples where sensitivity to the mass ordering is expected. The increased purity can be seen by comparing the FC multi-GeV single-ring e-like samples listed in Table III: The SK I–III multi-GeV $\bar{\nu}_e$-like sample requiring no decay electron has a MC purity of 34% true $\bar{\nu}_e$ CC interactions, while the SK IV–V multi-GeV $\bar{\nu}_e$-like sample requiring no decay electrons and one tagged neutron has a MC purity of 46% true $\bar{\nu}_e$ CC interactions.

Figure 13 shows a comparison of the sensitivities to the mass ordering and δ_{CP} obtained using the standard 19 samples discussed in Sec. II B for all SK phases versus the present configuration, which separates out the FC single-ring samples from the SK IV and SK V phases (approximately 57% of the total exposure) into additional samples which use neutron information. The figure demonstrates that using the neutron-tagged samples improves the expected sensitivity to the mass ordering and δ_{CP} by producing higher $\Delta\chi^2$ values [see Eq. (10)] away from the true oscillation parameters. Using the neutron-tagged samples has a negligible effect on the sensitivities to $\sin^2\theta_{23}$ and Δm^2_{32}, which are primarily constrained by the ν_μ-enriched samples.

E. Results

1. Atmospheric-only results

Results in this section and the next are presented as $\Delta\chi^2$ contours of one or two oscillation parameters taken with respect to the global best-fit point, with and without constraints on θ_{13}. The contours are profiled: We draw the minimum $\Delta\chi^2$ values among all other combinations of oscillation parameters scanned with one or two oscillation parameters fixed.

Figure 14 shows the one-dimensional (1D) $\Delta\chi^2$ contours in the atmospheric-only analyses for the fitted neutrino oscillation parameters δ_{CP}, $\sin^2\theta_{13}$, $\Delta m^2_{32,31}$, and $\sin^2\theta_{23}$, with respect to the best-fit point across both

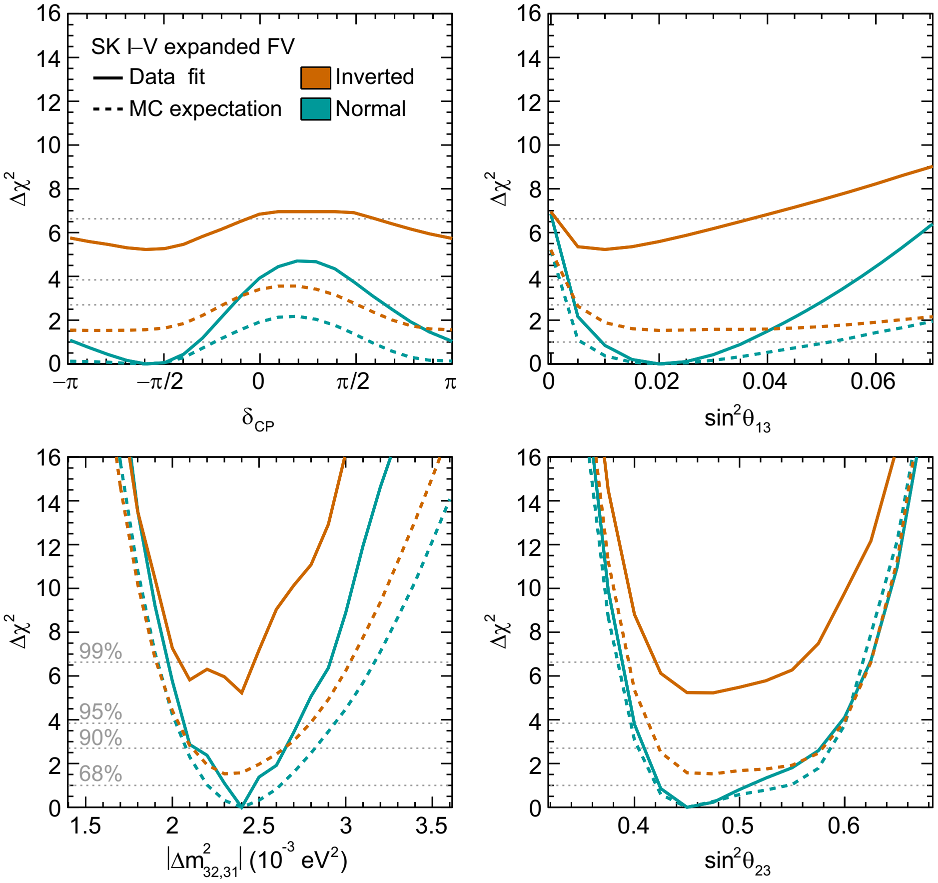

FIG. 14. 1D $\Delta\chi^2$ profiles of oscillation parameters in the analysis, with $\sin^2\theta_{13}$ treated as a free parameter. Solid lines correspond to the data fit result, while dashed lines correspond to the MC expectation at the data best-fit oscillation parameters, cf. Table IV. Dotted lines show critical values of the χ^2 distribution for 1 degree of freedom, with the lowest to highest corresponding to 68%, 90%, 95%, and 99% probabilities.

mass orderings. The normal ordering is preferred: The difference between the minimum χ^2 in the inverted and normal orderings is $\Delta\chi^2_{\mathrm{I.O.-N.O.}} = 5.23$. The MC expectation for the mass ordering at the best-fit oscillation parameters is $\Delta\chi^2_{\mathrm{I.O.-N.O.}} = 1.53$, indicated by dashed lines in Fig. 14. The difference between the data result and the MC expectation is discussed in Sec. V.

Sensitivity to δ_{CP} in the SK data originates from both sub-GeV and multi-GeV *e*-like samples, where values of δ_{CP} near $-\pi/2$ indicate increased ν_e appearance and decreased $\bar{\nu}_e$ appearance relative to $\delta_{\mathrm{CP}} = 0$. The best-fit value of δ_{CP} is -1.89 in both orderings, signaling increased ν_e appearance. The constraints on δ_{CP} and $\sin^2\theta_{13}$ assuming the inverted ordering are weaker, although consistent with the best-fit values assuming the normal ordering. These weaker constraints are an expected consequence of the freedom to adjust $\sin^2\theta_{13}$ and δ_{CP} simultaneously, combined with the reduced antineutrino statistics relative to neutrino statistics in the atmospheric neutrino data.

The preferred values of $\sin^2\theta_{13}$ are 0.020 and 0.010 in the normal ordering and inverted ordering, respectively. Both results are consistent with the reactor-preferred value of $\sin^2\theta_{13} = 0.0220$ at the 90% confidence level, and $\sin^2\theta_{13} = 0$ is disfavored in the normal ordering at the 99% level. The data favor the magnitude of the fitted squared-mass difference $|\Delta m^2_{32,31}| = 2.40 \times 10^{-3}\ \mathrm{eV}^2$ in both orderings. The nonsmooth behavior of the constraints on this parameter, especially evident in the inverted ordering fit, is a consequence of rapidly varying oscillation probabilities in the sub-GeV samples. Finally, the atmospheric neutrino data place the best-fit value of $\sin^2\theta_{23}$ in the lower octant, $\sin^2\theta_{23} = 0.45$, although values in each octant are allowed at the 68% level.

As discussed in Sec. I A, the combination of nonzero $\sin^2\theta_{13}$ and a normal neutrino mass ordering leads to electron neutrino appearance for upward-going multi-GeV events. We observe excess electron-flavor upward-going multi-GeV single-ring and multi-ring events in the SK data.

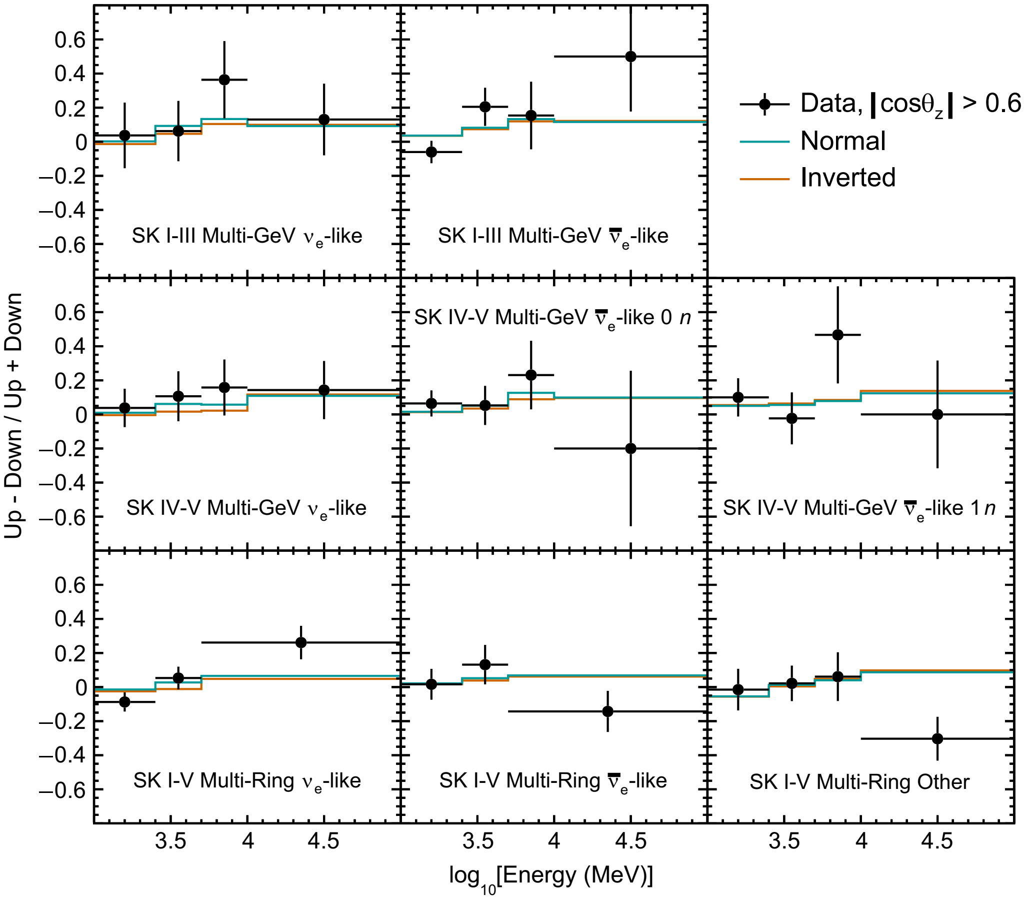

FIG. 15. Up-down asymmetry for multi-GeV *e*-like events. The *y* axis is the asymmetry parameter, the ratio between the difference and sum of upward-going ($\cos\theta_z < 0.6$) and downward-going ($\cos\theta_z > 0.6$) events. The *x* axis is the reconstructed neutrino energy: For single-ring events, the reconstructed energy is the visible energy of the ring assuming the reconstructed ring is an electron, while for mult-iring events, it is the total visible energy of the event. All error bars are statistical. MC lines for the normal and inverted orderings are drawn assuming the best-fit oscillation parameters of the analysis with $\sin^2\theta_{13}$ constrained. SK IV-V multi-GeV single-ring events are selected using the number of tagged neutrons, and so they are separated from the SK I–III multi-GeV single-ring samples.

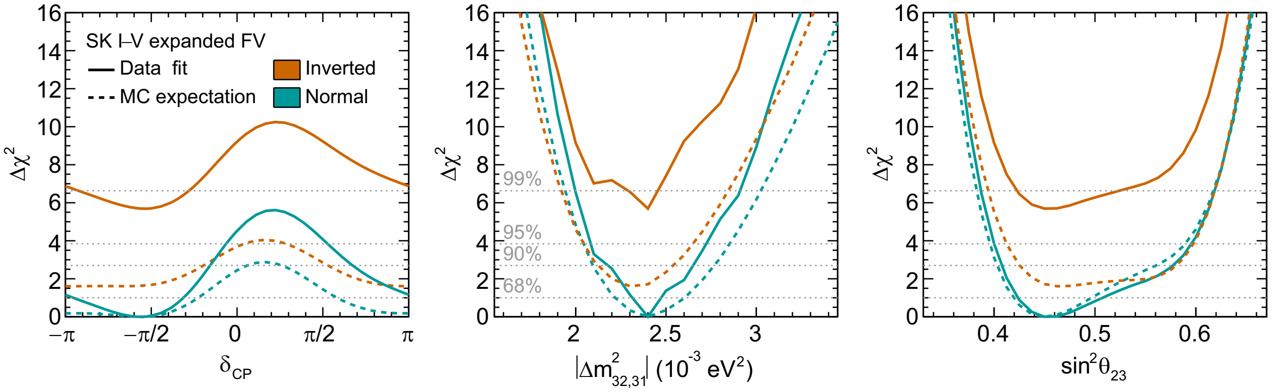

FIG. 16. 1D $\Delta\chi^2$ profiles of oscillation parameters in the analysis with $\sin^2\theta_{13}$ constrained. Solid lines correspond to the data fit result, while dashed lines correspond to the MC expectation at the data best-fit oscillation parameters, cf. Table IV. Dotted lines show critical values of the χ^2 distribution for 1 degree of freedom corresponding to 68%, 90%, 95%, and 99% probabilities.

Figure 15 shows a projection of the multi-GeV e-like samples as an up-down asymmetry

$$\text{Asymmetry} = \frac{\text{Up} - \text{Down}}{\text{Up} + \text{Down}}, \tag{12}$$

where "Up" is the number of upward-going ($\cos\theta_z < -0.6$) events, and "Down" is the number of downward-going ($\cos\theta_z > 0.6$) events in each sample. The figure plots the asymmetry for these data as a function of reconstructed energy and the expected asymmetry for the normal and inverted ordering scenarios, assuming the best-fit oscillation parameters from the fit to all atmospheric neutrino data. The ν_e-enhanced samples, multi-GeV ν_e-like and multi-ring ν_e-like, have the largest excesses relative to either ordering, and drive the preference for the normal mass ordering in the analysis.

2. *Results with reactor constraints on* $\sin^2\theta_{13}$

Figure 16 shows the 1D $\Delta\chi^2$ profiles for the fitted neutrino oscillation parameters, assuming the constraint $\sin^2\theta_{13} = 0.0220 \pm 0.0007$ from reactor antineutrino disappearance experiments [31]. The constraint on $\sin^2\theta_{13}$ is incorporated by introducing an additional systematic uncertainty for this fit, where the 1σ effect is defined as the change induced by varying $\sin^2\theta_{13}$ by its measured 1σ uncertainty.

The best-fit value of δ_{CP} in both the normal and inverted orderings for the fit with $\sin^2\theta_{13}$ constrained is -1.75, which is consistent with the atmospheric-only analysis at the 1σ level. This fit also finds improved constraints on δ_{CP} in the inverted ordering for values near $\pi/2$: The constraint on $\sin^2\theta_{13}$ fixes the effect size of the mass ordering, such that the separate modifications to ν_e appearance from δ_{CP} are more readily resolved.

In this fit, the preference for the normal ordering increases to $\Delta\chi^2_{\text{I.O.}-\text{N.O.}} = 5.69$. This improvement is consistent with the observed preference for smaller values of $\sin^2\theta_{13}$ in the inverted ordering fit with $\sin^2\theta_{13}$ free: The χ^2 value in the inverted ordering increases with the added constraint, while the χ^2 value in the normal ordering remains similar to the result without the constraint.

Figure 17 shows the constraints on $\sin^2\theta_{23}$ and Δm^2_{32} from the θ_{13}-constrained analysis of SK atmospheric neutrino data compared with the constraints from MINOS/MINOS+ [53], NOvA [4], T2K [3], and IceCube [54]. The SK atmospheric neutrino data are consistent with the other experiments at the 90% level. While the atmospheric neutrino data find a best-fit value of $\sin^2\theta_{23}$ in the lower octant, we note that the previous publication found a best-fit value in the upper octant [5], and

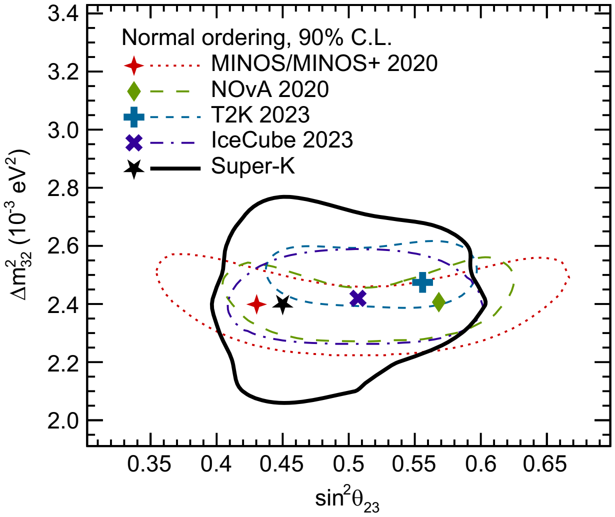

FIG. 17. 2D constant $\Delta\chi^2$ contours of neutrino oscillation parameters Δm^2_{32} and $\sin^2\theta_{23}$ for the normal mass ordering. Contours are drawn for a 90% critical χ^2 value assuming 2 degrees of freedom, with the $\Delta\chi^2$ computed for each experiment with respect to the best-fit point in the normal mass ordering. The Super-K contour shows the result of this analysis, and other contours are adapted from publications by MINOS+ [53], NOvA [4], T2K [3], and IceCube [54]. Best-fit points are indicated with markers for each experiment.

TABLE V. Best-fit neutrino oscillation parameters from the analyses presented in this work. The uncertainties on each oscillation parameter are the $\pm 1\sigma$ allowed regions assuming a χ^2 distribution with 1 degree of freedom. The second-to-last column shows the total χ^2. Both analyses have 930 bins.

Fit result	Ordering	$\lvert\Delta m^2_{32,31}\rvert$ (10^{-3} eV^2)	$\sin^2\theta_{23}$	$\sin^2\theta_{13}$	δ_{CP} $(-\pi,\pi)$	χ^2	$\Delta\chi^2_{\mathrm{I.O.-N.O.}}$
SK, Atmospheric only	Normal	$2.40^{+0.07}_{-0.09}$	$0.45^{+0.06}_{-0.03}$	$0.020^{+0.016}_{-0.011}$	$-1.89^{+0.87}_{-1.18}$	1022.06	5.23
	Inverted	$2.40^{+0.05}_{-0.33}$	$0.48^{+0.07}_{-0.05}$	$0.010^{+0.021}_{-0.008}$	$-1.89^{+1.32}_{-1.97}$	1027.29	
SK, $\sin^2\theta_{13}$ Constrained	Normal	$2.40^{+0.07}_{-0.09}$	$0.45^{+0.06}_{-0.03}$	...	$-1.75^{+0.76}_{-1.25}$	1022.06	5.69
	Inverted	$2.40^{+0.06}_{-0.12}$	$0.45^{+0.08}_{-0.03}$	...	$-1.75^{+0.89}_{-1.22}$	1027.75	

that values of $\sin^2\theta_{23}$ in both octants are allowed at the 1σ level.

V. INTERPRETATION

Table V summarizes the fit results of the analyses presented in this work. In both analyses, the normal ordering is preferred, and the best-fit oscillation parameters predict weaker sensitivities to the neutrino mass ordering than the observed $\Delta\chi^2_{\mathrm{I.O.-N.O.}}$. To quantify the significance of the mass-ordering preference from the fit results, we generated ensembles of toy datasets to produce the distribution of the $\Delta\chi^2_{\mathrm{I.O.-N.O.}}$ statistic.[3] Each toy dataset consists of fluctuated counts according to each bin's statistical uncertainty, which are scaled by randomly sampling the systematic uncertainty coefficients. Ensembles were generated assuming both the normal and inverted mass orderings and with oscillation parameters fixed at the best-fit points. We fit each toy dataset in each ordering with Δm^2_{32}, $\sin^2\theta_{23}$, and δ_{CP} as free parameters to compute $\Delta\chi^2_{\mathrm{I.O.-N.O.}}$.

Figure 18 shows the distribution of $\Delta\chi^2_{\mathrm{I.O.-N.O.}}$ compared with the data fit result for the atmospheric analysis with $\sin^2\theta_{13}$ constrained. The probability of observing a more extreme result than the data (the p-value) is given by the area to the right of the data line in the normal-ordering scenario, and by the area to the left of the data line in the inverted-ordering scenario. While the figure shows the p-value determined from simulated datasets for the inverted mass ordering is 0.0091, we note that with the present SK statistics, the expected sensitivity remains weak for rejecting either ordering. Indeed, the p-value for the data result within the normal ordering, 0.88, is not especially likely either. For the situation in which the data must select between two mutually exclusive hypotheses, the CL$_s$ method [56] provides an estimate of the p-value that considers simultaneous agreement from both hypotheses:

$$\mathrm{CL}_s = \frac{p_{\mathrm{I.O.}}}{1 - p_{\mathrm{N.O.}}}, \tag{13}$$

where $p_{\mathrm{N.O.}}$ and $p_{\mathrm{I.O.}}$ refer to the p-values in the normal or inverted ordering. This prescription decreases the significance for rejecting the inverted hypothesis proportional to the simultaneous significance of accepting the normal-ordering hypothesis. The CL$_s$ for the atmospheric analysis with $\sin^2\theta_{13}$ constrained is 0.077, corresponding to a rejection of the inverted mass ordering at the 92.3% confidence level. This number is similar to the previous SK result, CL$_s = 0.070$ [5], despite originating from a larger $\Delta\chi^2$, 5.69 versus 4.33. While the mass-ordering sensitivity and data result both increased for this analysis, the probability of obtaining the data result simultaneously decreased in both orderings, resulting in a similar CL$_s$ value.

The p-value obtained from toy datasets depends on the choice of oscillation parameters. While the atmospheric analysis places $\sin^2\theta_{23}$ in the lower octant, values of $\sin^2\theta_{23}$ spanning both octants are allowed at the 1σ level.

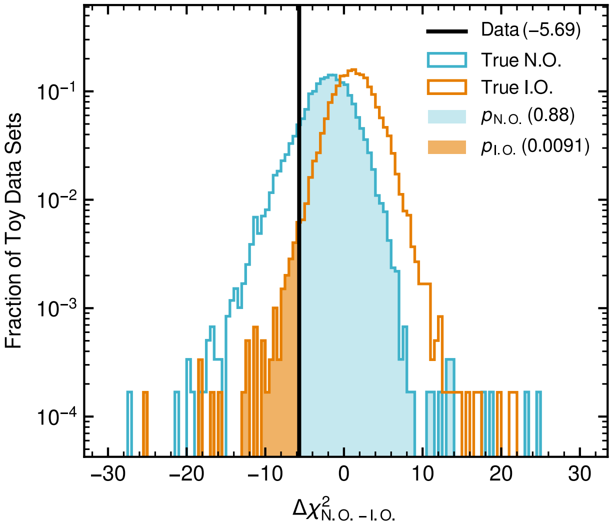

FIG. 18. Distribution of the mass-ordering preference statistic, $\Delta\chi^2_{\mathrm{I.O.-N.O.}}$, for ensembles of simulated datasets, assuming either the normal or inverted mass orderings. The data result from the atmospheric analysis with $\sin^2\theta_{13}$ constrained is shown as the vertical black line. The blue and orange histograms indicate the distribution of this statistic for toy datasets assuming the normal and inverted ordering, respectively. The filled areas to the left of the data result for inverted toy datasets and to the right of the data result for normal toy datasets indicate the p-values.

---

[3] Because the two mass-ordering scenarios are not nested hypotheses, taking the square root of $\Delta\chi^2_{\mathrm{I.O.-N.O.}}$ to estimate the significance by invoking Wilks' theorem is not recommended [55].

Larger values of $\sin^2\theta_{23}$ and δ_{CP} values near $-\pi/2$ increase the sensitivity of SK for rejecting the incorrect mass ordering, since they enhance the $\nu_\mu \to \nu_e$ signal. Accordingly, the mass ordering is more difficult to resolve for smaller values of $\sin^2\theta_{23}$ and values of δ_{CP} near $\pi/2$. To demonstrate the dependence of CL_s outcomes on the choice of oscillation parameters, we repeated the generation of toy datasets for configurations of oscillation parameters which maximize and minimize the expected sensitivity to rejecting the incorrect mass ordering and are allowed at the 90% confidence level. The range of CL_s values obtained in the atmospheric fit with $\sin^2\theta_{13}$ constrained spans 0.033–0.220. We observe that upper-octant values of $\sin^2\theta_{23}$ predict larger $\Delta\chi^2_{\mathrm{I.O.-N.O.}}$ values which are closer to the observed data result. We anticipate that better constraints on the $\sin^2\theta_{23}$ octant will reduce the difference between the $\Delta\chi^2_{\mathrm{I.O.-N.O.}}$ values expected from MC and obtained from data.

VI. CONCLUSION

We analyzed 6511.3 live days of atmospheric neutrino data collected with the Super-Kamiokande experiment operating with pure water and an expanded fiducial volume. An event selection using tagged neutron information was used to enhance the statistical separation of neutrino and antineutrino data, thereby increasing the sensitivity to the neutrino mass ordering. An analysis of SK data with constraints on $\sin^2\theta_{13}$ measures the oscillation parameters to be $\Delta m^2_{32} = 2.40^{+0.07}_{-0.09} \times 10^{-3}\ \mathrm{eV}^2$, $\sin^2\theta_{23} = 0.45^{+0.06}_{-0.03}$, and $\delta_{\mathrm{CP}} = -1.75^{+0.76}_{-1.25}$. The analysis prefers the normal ordering over the inverted ordering at the 92.3% confidence level. We anticipate improvements to the mass-ordering sensitivity in future analyses of SK atmospheric data which include gadolinium-enhanced neutron tagging for enhanced neutrino and antineutrino separation.

This work is accompanied by a data release [57]. The data release contains the 1D and 2D contours of fitted oscillation parameters at the 68% and 90% confidence levels from the analyses described in Sec. IV, and listings of the data and MC counts in the 930 atmospheric neutrino bins used throughout this work. Summary statistics of the MC neutrino energies, directions, and flavors are provided for each bin.

ACKNOWLEDGMENTS

We gratefully acknowledge the cooperation of the Kamioka Mining and Smelting Company. The Super-Kamiokande experiment has been built and operated from funding by the Japanese Ministry of Education, Culture, Sports, Science and Technology, the U.S. Department of Energy, and the U.S. National Science Foundation. Some of us have been supported by funds from the National Research Foundation of Korea (NRF-2009-0083526 and NRF 2022R1A5A1030700) funded by the Ministry of Science, Information, and Communication Technology (ICT), the Institute for Basic Science (IBS-R016-Y2), and the Ministry of Education (2018R1D1A1B07049158, 2021R1I1A1A01042256); the Japan Society for the Promotion of Science, the National Natural Science Foundation of China under Grant No. 11620101004; the Spanish Ministry of Science, Universities and Innovation (Grant No. PGC2018-099388-B-I00); the Natural Sciences and Engineering Research Council (NSERC) of Canada, the Scinet and Westgrid consortia of Compute Canada; the National Science Centre (UMO-2018/30/E/ST2/00441 and UMO-2022/46/E/ST2/00336) and the Ministry of Education and Science (2023/WK/04), Poland; the Science and Technology Facilities Council (STFC) and Grid for Particle Physics (GridPP), United Kingdom; the European Union's Horizon 2020 Research and Innovation Programme under Marie Sklodowska-Curie Grant Agreement No. 754496, H2020-MSCA-RISE-2018 JENNIFER2 Grant agreement No. 822070, H2020-MSCA-RISE-2019 SK2HK Grant Agreement No. 872549, and H2020-MSCA-GF-2019 HYPER-KOD Grant Agreement No. 892264.

[1] B. Pontecorvo, Zh. Eksp. Teor. Fiz. **53**, 1717 (1967).
[2] Z. Maki, M. Nakagawa, and S. Sakata, Prog. Theor. Phys. **28**, 870 (1962).
[3] K. Abe *et al.* (T2K Collaboration), Eur. Phys. J. C **83**, 782 (2023).
[4] M. Acero *et al.* (NOvA Collaboration), Phys. Rev. D **106**, 032004 (2022).
[5] K. Abe *et al.* (Super-Kamiokande Collaboration), Phys. Rev. D **97**, 072001 (2018).
[6] D. Adey *et al.* (Daya Bay Collaboration), Phys. Rev. Lett. **121**, 241805 (2018).
[7] C. D. Shin *et al.* (RENO Collaboration), J. High Energy Phys. 04 (2020) 29.
[8] H. de Kerret *et al.* (Double-Chooz Collaboration), Nat. Phys. **16**, 558 (2020).
[9] Q. R. Ahmad, R. C. Allen *et al.* (SNO Collaboration), Phys. Rev. Lett. **87**, 071301 (2001).
[10] S. Fukuda *et al.* (Super-Kamiokande Collaboration), Phys. Rev. Lett. **86**, 5651 (2001).
[11] L. Wolfenstein, Phys. Rev. D **17**, 2369 (1978).
[12] S. P. Mikheev and A. Yu Smirnov, Nuovo Cim. C **9**, 17 (1986).

[13] A. M. Dziewonski and D. L. Anderson, Phys. Earth Planet. Inter. **25**, 297 (1981).

[14] V. Barger, K. Whisnant, S. Pakvasa, and R. J. N. Phillips, Phys. Rev. D **22**, 2718 (1980).

[15] S. Fukuda *et al.*, Nucl. Instrum. Methods Phys. Res., Sect. A **501**, 418 (2003).

[16] K. Abe *et al.* (Super-Kamiokande Collaboration), Nucl. Instrum. Methods Phys. Res., Sect. A **737**, 253 (2014).

[17] A. Suzuki, M. Mori, K. Kaneyuki, T. Tanimori, J. Takeuchi, H. Kyushima, and Y. Ohashi, Nucl. Instrum. Methods Phys. Res., Sect. A **329**, 299 (1993).

[18] H. Nishino, K. Awai, Y. Hayato, S. Nakayama, K. Okumura, M. Shiozawa, A. Takeda, K. Ishikawa, A. Minegishi, and Y. Arai, Nucl. Instrum. Methods Phys. Res., Sect. A **610**, 710 (2009).

[19] S. Yamada *et al.*, IEEE Trans. Nucl. Sci. **57**, 428 (2010).

[20] K. Abe *et al.* (Super-Kamiokande Collaboration), Nucl. Instrum. Methods Phys. Res., Sect. A **1027**, 166248 (2022).

[21] M. Shiozawa, Nucl. Instrum. Methods Phys. Res., Sect. A **433**, 240 (1999).

[22] K. Abe *et al.* (Super-Kamiokande Collaboration), J. Instrum. **17**, P10029 (2022).

[23] P. F. Menéndez, Neutrino physics in present and future Kamioka water-Čerenkov detectors with neutron tagging, Ph.D. thesis, Autonomous University of Madrid, 2017.

[24] R. Wendell *et al.* (Super-Kamiokande Collaboration), Phys. Rev. D **81**, 092004 (2010).

[25] R. Matsumoto, Development of an atmospheric event classification method for Super-Kamiokande, Master's thesis, Tokyo University of Science, 2020.

[26] A. Takenaka *et al.* (Super-Kamiokande Collaboration), Phys. Rev. D **102**, 112011 (2020).

[27] M. Honda, T. Kajita, K. Kasahara, and S. Midorikawa, Phys. Rev. D **83**, 123001 (2011).

[28] Y. Hayato, Nucl. Phys. B Proc. Suppl. **112**, 171 (2002).

[29] Y. Hayato and L. Pickering, Eur. Phys. J. Spec. Top. **230**, 4469 (2021).

[30] R. Brun, F. Bruyant, F. Carminati, S. Giani, M. Maire, A. McPherson, G. Patrick, and L. Urban, GEANT: Detector Description and Simulation Tool; Oct 1994, CERN Program Library (CERN, Geneva, 1993), long Writeup W5013, https://inspirehep.net/literature/863473.

[31] R. L. Workman *et al.* (Particle Data Group), Prog. Theor. Exp. Phys. **2022**, 083C01 (2022).

[32] R. Smith and E. Moniz, Nucl. Phys. **B43**, 605 (1972).

[33] J. Nieves, I. R. Simo, and M. J. V. Vacas, Phys. Rev. C **83**, 045501 (2011).

[34] J. Nieves *et al.*, Nucl. Part. Phys. Proc. **273–275**, 1830 (2016).

[35] R. Bradford, A. Bodek, H. Budd, and J. Arrington, Nucl. Phys. B Proc. Suppl. **159**, 127 (2006).

[36] D. Rein and L. M. Sehgal, Ann. Phys. (N.Y.) **133**, 79 (1981).

[37] C. Berger and L. M. Sehgal, Phys. Rev. D **76**, 113004 (2007).

[38] P. Martins, Charged current coherent pion production in neutrino scattering, arXiv:1605.00095.

[39] M. Glück, E. Reya, and A. Vogt, Eur. Phys. J. C **5**, 461 (1998).

[40] A. Bodek and U. Yang, AIP Conf. Proc. **792**, 257 (2005).

[41] T. Sjöstrand, Comput. Phys. Commun. **82**, 74 (1994).

[42] E. S. Pinzon Guerra *et al.* (DUET Collaboration), Phys. Rev. C **95**, 045203 (2017).

[43] R. Gran, J. Nieves, F. Sanchez, and M. J. Vacas, Phys. Rev. D **88**, 113007 (2013).

[44] T. Wester, Discerning the neutrino mass ordering using atmospheric neutrinos in Super-Kamiokande I–V, Ph.D. thesis, Boston University, 2023.

[45] M. Honda, T. Kajita, K. Kasahara, S. Midorikawa, and T. Sanuki, Phys. Rev. D **75**, 043006 (2007).

[46] K. Abe *et al.* (T2K Collaboration), Phys. Rev. D **91**, 072010 (2015).

[47] R. Akutsu, A study of neutrons associated with neutrino and antineutrino interactions on the water target at the T2K far detector, Ph.D. thesis, University of Tokyo, 2020.

[48] C. Andreopoulos *et al.*, Nucl. Instrum. Methods Phys. Res., Sect. A **614**, 87 (2010).

[49] K. Abe *et al.* (Super-Kamiokande Collaboration), Phys. Rev. Lett. **110**, 181802 (2013).

[50] K. Hagiwara, K. Mawatari, and H. Yokoya, Nucl. Phys. **B668**, 364 (2003).

[51] H. Watanabe *et al.*, Astropart. Phys. **31**, 320 (2009).

[52] Z. Li *et al.* (Super-Kamiokande Collaboration), Phys. Rev. D **98**, 052006 (2018).

[53] P. Adamson *et al.* (MINOS+ Collaboration), Phys. Rev. Lett. **125**, 131802 (2020).

[54] R. Abbasi *et al.* (IceCube Collaboration), Phys. Rev. D **108**, 012014 (2023).

[55] S. Algeri, J. Aalbers, K. D. Morå, and J. Conrad, Nat. Rev. Phys. **2**, 245 (2020).

[56] A. L. Read, J. Phys. G **28**, 2693 (2002).

[57] Data release: Atmospheric neutrino oscillation analysis with neutron tagging and an expanded fiducial volume in Super-Kamiokande I–V, 10.5281/zenodo.8401262 (2023).